NuSTAR observations of 4U 0115+63

Bachelorarbeit aus der Physik

vorgelegt von

Katrin Berger

15.02.2019

Astronomisches Institut Dr. Karl Remeis-Sternwarte

Friedrich-Alexander-Universität Erlangen-Nürnberg

Department Physik

Betreuer: Prof. Dr. Jörn Wilms

Abstract

This work contains the analysis of the spectra and light curve of two NuSTAR observations of the X-ray binary system 4U 0115+63 taken during the peak and decay of its 2015 November outburst. The time-averaged spectrum was fitted with an empirical powerlaw model with exponential cutoff which is typically used for this kind of sources and which as been successfully applied in previous analyses. A broad, Gaussian emission feature centered around ~8.5 keV was needed for a good description of the NuSTAR data. Furthermore, the spectra of both observations show three Cyclotron Resonant Scattering Features (CRSFs) at 11 keV, 23 keV, and 34 keV, which are identified as the fundamental and two harmonic lines. The presence of two fundamental CRSFs of slightly different energy, that were proposed in the literature, could not be confirmed.

Beside its 3.6 s pulse period, 4U 0115+63 shows a strong ~600 s quasi periodic oscillation. The pulse arrival times were identified from the light curve and their periodicity was analysed with the intention to define QPO phases suitable for spectroscopy. This definition was strongly affected by irregularities in the light curve, e.g., asymmetric pulses, flaring, and missing pulses.

Investigations of the evolution of the hardness ratio with time showed that spectral changes mostly happened during strong QPO pulses, so those were selected manually for time-resolved spectroscopy. Furthermore, the hardness ratios indicated that the 7–15 keV energy range was most affected by these spectral changes. Fits of the empirical model to the time-resolved spectra indeed showed that most of the spectral variability can be accounted for by re-scaling the flux of the Gaussian emission component with respect to the continuum flux. The flux ratios of the flux of the 10 keV-feature compared to the flux of the powerlaw vary up to ~20% during the peak and off-peak states with respect to the observation-averaged spectrum.

These results are discussed in the context of existing observations and models of spectral formation in accretion columns.

Contents

1. Introduction

Beside black holes and white dwarfs, neutron stars are a possible state a high mass star can end its life in. They are small objects, with a radius around 10 km and a mass of about 1.5 times the mass of our sun. Therefore they are not only one of the densest objects in space, but are also the origin of some of the strongest magnetic fields with strengths exceeding 10^{13} Gauss (Lattimer & Prakash, 2004). For comparison, CERN reported in 2013 to have tested new magnets, that were able to generate a magnetic field with a strength of 13.5 Tesla, i.e., 1.35×10^5 Gauss (Charley, 2013). A new record was set in 2018 by a team of scientists in Japan. They were able to create a magnetic field in their laboratory with a peak strength of 1200 Tesla (Nakamura et al., 2018). Up to now the characteristic properties of neutron stars cannot be reproduced artificially and they provide a unique laboratory for extreme conditions.

A specific class of sources are neutron stars in binary system with a companion star. The companion star can donate matter that is accreted onto the neutron star (Müller et al., 2013) which provides one of the most efficient sources of energy in the universe. These systems are therefore often very bright X-ray sources (Becker et al., 2012) and observations of these X-rays can be used to study the behavior of matter in the presence of strong magnetic fields and relativistic effects.

Despite decades of observations of neutron star binaries, many aspects of these sources are still poorly understood. One of the systems that has a long history of observations with many different X-ray telescopes, but is still subject of current research, is 4U 0115+63. In 2015, NASA's X-ray observatory NuSTAR observed this source twice to answer remaining questions about the magnetic field configuration, the accretion flow, and radiative processes close to the neutron star. This thesis focuses on the analysis of these data with a special interest in the spectral variability during the observation.

2. Accreting Neutron Stars

Stars develop differently over their lifespan depending on their initial mass $M_{\rm init}$ (Iben, 1991). Considering this criterion stars can be divided into four groups: very low mass ($M_{\rm init} \lesssim 0.5\,M_\odot$), low mass ($0.5\,M_\odot \lesssim M_{\rm init} \lesssim 2.3\,M_\odot$), intermediate mass ($2.3\,M_\odot \lesssim M_{\rm init} \lesssim 8\,M_\odot$), and high mass ($M_{\rm init} \gtrsim 8\,M_\odot$) stars. Here the mass of the sun $M_\odot$ was used to relate the stars masses to a common value (Clayton, 1968).
The less massive stars, with initial masses up to $\sim 8\,M_\odot$, are able to burn hydrogen to helium and almost all ignite helium burning (Girardi et al., 2000). However, their temperatures are too low to burn carbon or other heavier elements and therefore turn into 'white dwarfs' after burning all their fuel. An additional criterion for the formation is that the mass of the remnant does not exceed the Chandrasekhar-limit (Iben, 1991).
High mass stars on the other hand reach core temperatures high enough to ignite advanced burning stages, e.g., carbon and silicon burning. Finally this leads to an eruptive explosion, also known as a core-collapse supernova, at the end of their life leaving either an neutron star or a black hole as a remnant (Iben, 1991). The essential information to determine which case occurs is again coupled to the mass of the remaining object. Analog to a white dwarf's mass limit the maximum mass a neutron star can achieve is set by the Tolman–Oppenheimer–Volkoff limit.

2.1. X-ray binary systems

X-ray binary systems were first discovered in 1962 (Giacconi et al., 1962) and the first X-ray binary pulsars were detected by Giacconi et al. (1971) and Tananbaum et al. (1972). They are nowadays known to be some of the brightest X-ray sources on the sky (Becker et al., 2012). They can be classified into three categories regarding the mass of the donor star, not the mass of the compact object: the low mass, intermediate mass, and high mass X-ray binary systems (Schwarm, 2017). A prime example for a low mass X-ray binary is the system Her X-1 which consists of a $\sim$1.4 $M_\odot$ neutron star (NS) and a $\sim$2.2 $M_\odot$ A/F main sequence star (Crampton, 1974; Deeter et al., 1981). In systems like these, mass transfer happens mostly via Roche lobe overflow providing a rather persistent mass reservoir. In high mass X-ray binaries, the neutron star mostly accretes matter from the strong stellar wind of the massive companion (e.g, Vela X-1, Grinberg et al., 2017) or from the circumstellar disk of a Be-type star. 4U 0115+63, the system studied in this work, is of the latter type which are generally referred to as Be X-ray binaries (BeXRBs). They often show a transient behavior according to their binary orbit and the evolution of the Be disk (Shaw & Charles, 2013).
Angular momentum conservation of the transferred material leads to the formation of an accretion disc around the neutron star. Closer to the neutron star, the accretion flow is also governed by the strong magnetic field, up to the Alfvén radius, where the pressure of the magnetic field reaches a level comparable to the ram pressure of the particles in the accretion disc.
The Alfvén radius $R_{\rm A}$ can be determined using (Becker et al., 2012)

$$R_{\rm A} = 2.73\times10^{7}\,{\rm cm}\left(\frac{\Lambda}{0.1}\right)\times\left(\frac{M_\star}{1.4\,M_\odot}\right)^{1/7}\times\left(\frac{R_\star}{10\,{\rm km}}\right)^{10/7}\times\left(\frac{B_\star}{10^{12}\,{\rm G}}\right)^{4/7}\times\left(\frac{L_{\rm x}}{10^{37}\,{\rm erg\,s^{-1}}}\right)^{-2/7}$$

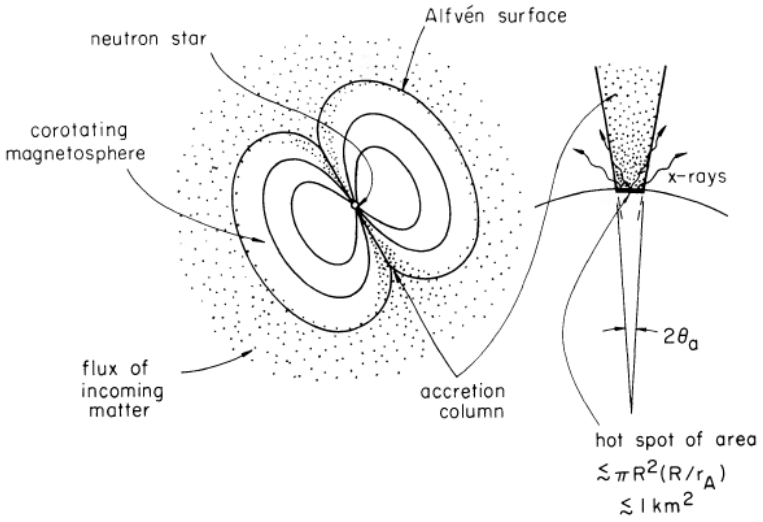

Figure 1: The figure illustrates the fundamental characteristics of the accretion of matter onto a neutron star. The left side shows the position of the Alfvén surface, with a distance of the Alfvén radius to the NS, the flow of the accreted matter, and the location of the accretion columns above the magnetic poles. The right side shows a close-up of an accretion column close to the surface of the NS (Lamb et al., 1973, Fig.1).

with the constant Λ describing the coupling of the matter to the magnetosphere ($\Lambda = 1$ in case of a spherical accretion and $\Lambda < 1$ for disk accretion), $M_\star$ and $R_\star$ the mass and radius of the NS, $B_\star$ the strength of the magnetic field at the surface of the NS, and L_x the X-ray luminosity. From this radius onward the accreted matter is channeled towards the magnetic poles of the star and forms accretion columns (Becker et al., 2012). A schematic picture is shown in Figure 1. The radiation of X-rays is produced by the decelerating matter inside the accretion column, where its kinetic energy is converted into radiation, which radiates away.

2.1.1. Quasi-periodic oscillations

A general feature seen in many NS low-mass X-ray binary systems are quasi-periodic oscillations (QPOs) (Motta et al., 2017). They can be identified as narrow peaks in a Fourier power density spectrum and appear combined with diverse components of broad-band noise. QPOs can be subdivided into low-frequency QPOs, observed in the range from a few mHz to ~ 60 Hz, and high-frequency QPOs, ranging from several hundred Hz up to frequencies $\gtrsim 1$ kHz in NS systems (Motta et al., 2017).
Although having first been observed 30 years ago (Soong & Swank, 1989) their origin is still unclear, but different models were developed to explain this effect. Possible explanations contain considerations of relativistic effects, another one might be that the low-frequency QPOs occur as a consequence of different instabilities or that they originate in oscillations of a boundary transition layer of matter, which was formed close to the compact object in the center (Motta et al., 2017). High-frequency QPOs on the other hand are explained by linking relativistic effects to orbital frequencies, or result in resonances between different frequencies

which appear in the accretion flow surrounding compact objects. Up to now the favored theory for fast spinning QPOs is the relativistic Lense-Thirring precession (Motta et al., 2017).

2.1.2. Cyclotron resonant scattering features

Most spectra from XRBPs contain absorption line-like, the so-called cyclotron resonant scattering features (CRSFs), or cyclotron lines. The first cyclotron line was discovered in the spectrum of the X-ray binary system Her X-1 by Trümper et al. (1978). At first it was unclear whether this line was created due to an absorption or emission effect. Specific studies regarding these cyclotron lines and their harmonics started in 1977, focusing on the emitting characteristics of this feature, until Nagel (1980) identified them to be absorption lines. Other objects are also considered to be possible sources of CRSFs, for example magnetars or gamma ray bursts, see (Schwarm, 2017) and references therein.
CRSFs are believed to originate in the strong magnetic fields around the poles of a NS. Due to the strong magnetic field at the poles of the neutron star the energy of the plasma electrons is quantized into Landau levels. Here CRSFs are formed if the continuum photons undertake resonant scatterings off these electrons. The magnetic field B at the location of formation is directly linked to the cyclotron energy E_{cyc} of the fundamental CRSF and can therefore be directly measured. The connection is given by the formula

$$E_{\mathrm{cyc}} = 11.58\,\mathrm{keV}\left(\frac{B}{10^{12}\,\mathrm{G}}\right),$$

where B is the magnetic field strength in Gauss. Harmonic CSRFs can occur at integer multiples of the fundamental line energy (Iyer et al., 2015; Becker et al., 2012).
Since the beginning of the research on CRSFs, possible processes that cause the variation of the line energy with luminosity and pulse phase have been discussed. Variations in the CRSF energy with luminosity originate in changes of the height of the line forming region inside the dipol magnetic field of the NS. Klochkov et al. (2008) showed that a variation of 25% of the energy of a CRSF detected in Her X-1 requires only a variation in height of about 1.1 km, when assuming a dipole magnetic field and a neutron star radius of 10 km.
The X-ray spectrum of an accreting pulsars can be described by a powerlaw with a high energy cutoff and additional absorption lines, the CRSFs (Müller et al., 2013). Many sources show additional emission components in the soft X-ray spectrum which are often modeled with a blackbody of temperatures of 1–2 keV or broad, Gaussian-shaped emission features around 8–10 keV, the so called "10 keV-feature" (Coburn, 2001). A representative spectrum can be seen in Figure 2.
Many accreting pulsars show only the fundamental CRSF or at most one harmonic. 4U 0115+63 shows a total of five CRSFs (Heindl et al., 2000). This is the highest number of harmonics seen in an XRBP so far, which makes this source very interesting for further inspections.

2.2. 4U 0115+63

The X-ray binary system 4U 0115+63 was first discovered in the sky survey performed by the satellite UHURU (Giacconi et al., 1972). It consists of a neutron star with a spin period

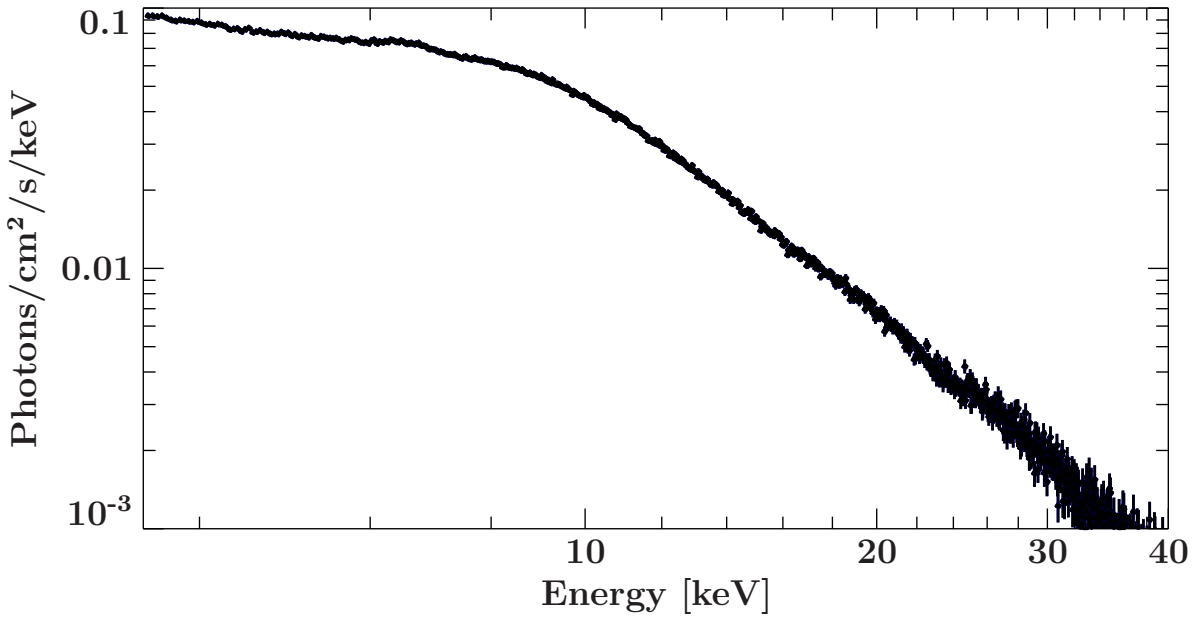

Figure 2: Spectrum of the neutron star 4U 0115+63.

of 3.61 s and an orbital period of 24.3 d around its companion O9e star V635 Cassiopeiae (Bildsten et al., 1997). The optical companion is a B0.2Ve star with an estimated distance of 7–8 kpc (Negueruela & Okazaki, 2001).
Up to now this source is the only one that shows four harmonic lines of the fundamental line. The CRSFs can be detected at energies of ~11 keV, ~22 keV, and ~33 keV (Iyer et al., 2015; Heindl et al., 1999). Recently, Iyer et al. (2015) claimed 4U 0115+63 actually exhibits two fundamental CRSFs, one at ~11 keV and another one at ~15 keV.
Beside the spin period, the light curve contains a second quasi-periodic variation with a period of ~ 600 s (Heindl et al., 1999).

2.3. NuSTAR

The observations used in this work were taken with the satellite NuSTAR. The 'Nuclear Spectroscopic Telescope Array' was launched on 2012 June 13 (Harrison et al., 2013) and is one of the Small Explorers (SMEX) missions of NASA. An artistic portrayal of the satellite is shown in Figure 3. NuSTAR is the first satellite that used a deployable mast that was extended in orbit to reach a focal length of 10 m. The scientific payload consists of two co-aligned conical Wolter-I approximation Optical Modules (OMA and OMB), each focusing onto one of the two solid-state Focal Plane Modules FPMA and FPMB, two CdZnTe-detectors. In combination with the large focal length, NuSTAR is the only focusing X-ray telescope sensitive up to ~80 keV. (Madsen et al., 2015; Harrison et al., 2013). The optics have a total field of view (FOV) of $13' \times 13'$ and the detectors are operating in the energy range from 3–79 keV and have an energy resolution of 0.4 keV at 10 keV and 0.9 keV at 60 keV (Harrison et al., 2013; Lotti et al., 2016). The energy resolution around the Fe Kα line is roughly a factor of 2–3 worse compared to standard CCD detectors (the energy resolution of Suzaku XIS was ~130 eV at

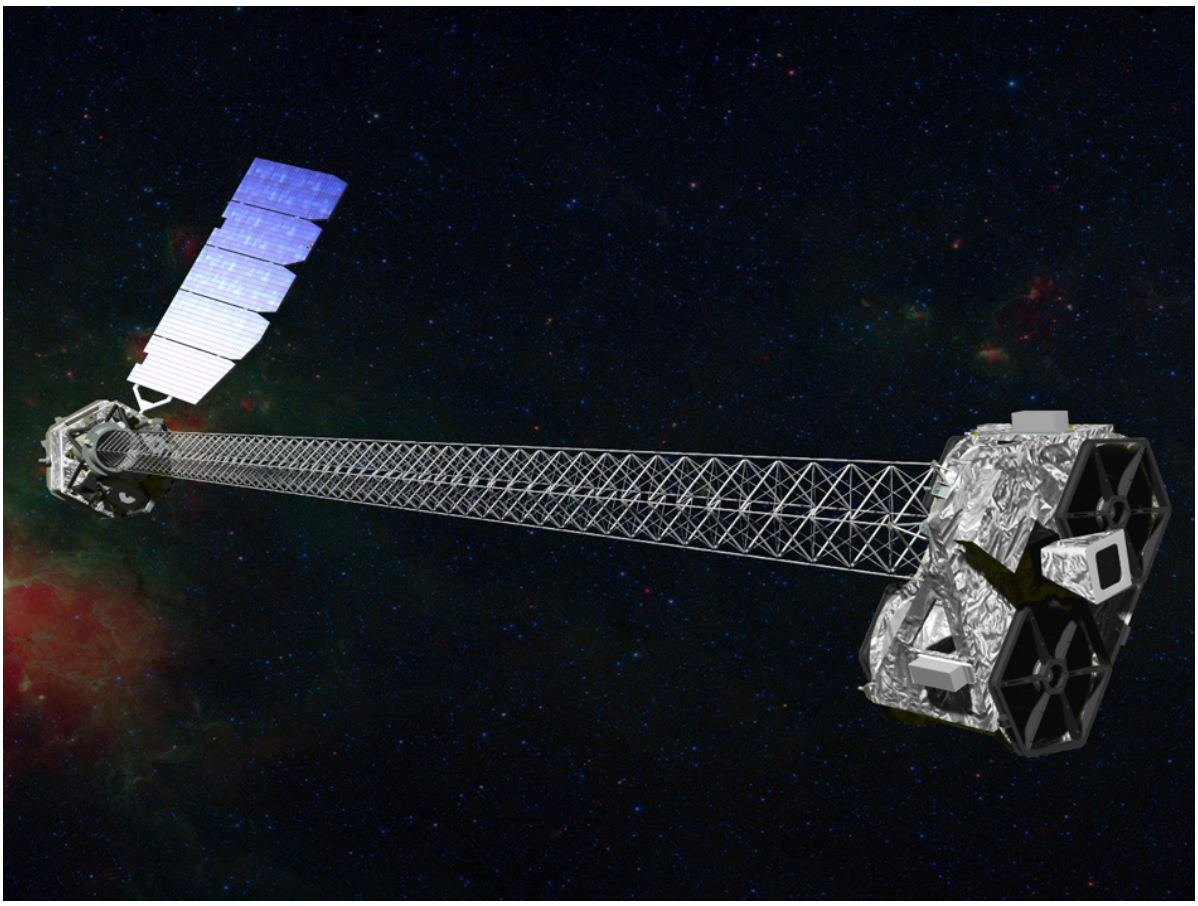

Figure 3: Artistic portrayal of the satellite NuSTAR in orbit. Image courtesy NASA/JPL-Caltech.

5.9 keV; Koyama et al., 2007).
The satellite was constructed to perform long-time observations with a duration from 1 day up to several weeks and to observe high-energy objects, such as black holes, supernovae, or neutron stars. Its key science programs include extra-galactic surveys to explore the activity of active galactic nuclei over cosmic time, galactic surveys to examine compact objects in the Milky Way, or observations of ultra-luminous X-ray sources (Harrison et al., 2013).
Observations from this satellite were chosen for this analysis because the imaging in the hard X-ray band involves a low background resulting in a good signal to noise ratio, supplying ideal requirements for CRSF measurements.

3. Data analysis: QPOs in 4U 0115+63

Previous analyses of 4U 0115+63 have mainly focused on characterizing the time-averaged broadband spectrum and the luminosity dependence of the CRSFs (e.g., Nakajima et al., 2006; Müller et al., 2013), the structure of the magnetic field inferred from the fundamental CRSF (Iyer et al., 2015), modeling the pulse profiles (Sasaki et al., 2012), the luminosity and energy dependence of the pulse profiles (Tsygankov & Lutovinov, 2007; Ferrigno et al., 2011), and most recently, the variability of the power spectral density (PSD) with time (Roy et al., 2019). As mentioned in the previous chapter, 4U 0115+63 shows a strong ~600 s QPO where the flux varies around 50%. The aim of this work is to analyze the spectral variability connected with the QPO.

I used two NuSTAR observations of 4U 0115+63 taken on 2015 October 30 for about 15 ks (ObsID: 90102016004, hereafter M1) and on 2015 October 22 with an effective observing time of 9 ks (ObsID: 90102016002, hereafter M2) which have been reprocessed using standard screening and calibration criteria with CALDB version 20180814 following the *The NuSTAR Data Analysis Software Guide*[1]. Extraction regions of the source and background are circles of 100″ radius which were chosen for each detector, FPMA and FPMB, individually. The source region was centered on the source, while the background region was placed in a corner of the observed image were no signal was detected.

For spectral fitting, I used the "Interactive Spectral Interpretation System" (ISIS) version 1.6.2-41.td2. Additionally, this research uses the ISIS functions (`ISISscripts`) provided by ECAP/Remeis observatory and MIT [2].

For the spectral analysis data from both detectors, FPMA and FPMB, were used in the energy range from 3.5 keV to 60 keV. The data below 3.5 keV are not sufficiently calibrated and above 60 keV the spectra are background-dominated. The spectra were rebinned to contain at least 25 counts per bin to justify the use of χ^2-statistics (Lampton et al., 1976; Gehrels, 1986). Furthermore, a minimum number of spectral channels were always binned to account for the decreasing energy resolution with increasing energy. The applied binning scheme is 2 bins up to 4 keV, 4 in the energy range from 4 keV to 9 keV, 8 from 9 keV to 15 keV, 15 up to 20 keV, and 20 from 20 keV to 40 keV.

3.1. Fitting the time-averaged spectrum

The fitting of the spectra of 4U 0115+63, which is shown in Figure 4, follows the procedure of Müller et al. (2013). The analysis was started with a basic cutoff powerlaw, selected with the command `CutoffPL` in ISIS, which is of the following shape:

$$\texttt{CutoffPL(E)} \propto E^{-\Gamma} \exp\left(-\frac{E}{E_{\text{fold}}}\right),$$

with the folding energy E_{fold} and the photon index Γ. Here data from both detectors, FPMA and FPMB, were used, which are real and no ideal instruments. To account for uncertainties

[1] `https://heasarc.gsfc.nasa.gov/docs/nustar/analysis/nustar_swguide.pdf`
[2] `http://www.sternwarte.uni-erlangen.de/isis/`

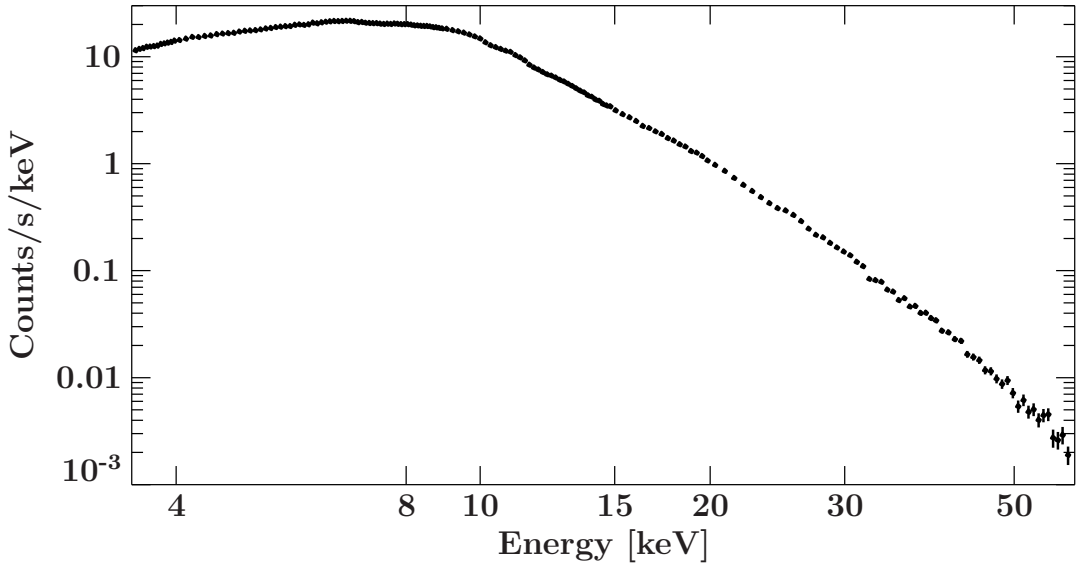

Figure 4: NuSTAR spectrum of the neutron star 4U 0115+63.

in the flux calibration a multiplicative detector constant, called `detconst`, was included. The resulting parameters are c_{FPMA} and c_{FPMB}. For all measurements the constant describing the detector FPMA was fixed to 1 leaving c_{FPMB} a free parameter. A preliminary fit of the pure `cutoffpl` model is shown in Figure 5 a) for observation $M1$ and Figure 16 for $M2$.
Although NuSTAR covers mostly the hard X-ray spectrum of 4U 0115+63, the soft part is affected by absorption in the Interstellar Medium (ISM). To account for this effect, the multiplicative model `tbnew`, an updated version of `tbabs` was included in the fit function. Abundances and cross sections were set according to Wilms et al. (2000) and Verner & Yakovlev (1995), respectively. Since NuSTAR is not sensitive below ~3 keV, the equivalent hydrogen absorption column density N_{H} could not be constrained and was therefore fixed to 1.5×10^{22} cm^{-2}, because typical values range from 1.3–1.7$\times 10^{22}$ cm^{-2} (Müller et al., 2013; Iyer et al., 2015, Kühnel et al., in prep.).
In order to model the Fe Kα fluorescence line at 6.4 keV, that occurs in the spectra, a Gaussian emission line (`egauss` in ISIS) of the form

$$A(E) = K \frac{1}{\sigma \cdot \sqrt{2\pi}} \exp\left(-\frac{(E - E_{\mathrm{l}})^2}{2\sigma^2}\right),$$

where E_{l}, σ, and K are the line energy, width, and scaling factor, respectively, was added to the model. Although the intrinsic line width is much smaller than the detector response the line broadening should only be caused by the detector response. 4U 0115+63 is known to show also emission lines of higher ionization states of iron, which cannot be resolved in NuSTAR but are modeled with a broad Gaussian line with a width of a few hundred eV.
Another broad Gaussian emission feature around 8.5 keV had to be added to the cutoff powerlaw, representing the 10 keV-feature, which has been observed in the spectra of 4U 0115+63 before (Coburn, 2001). The resulting fit is illustrated in Figure 5 b for $M1$ and in Figure 17 for $M2$.

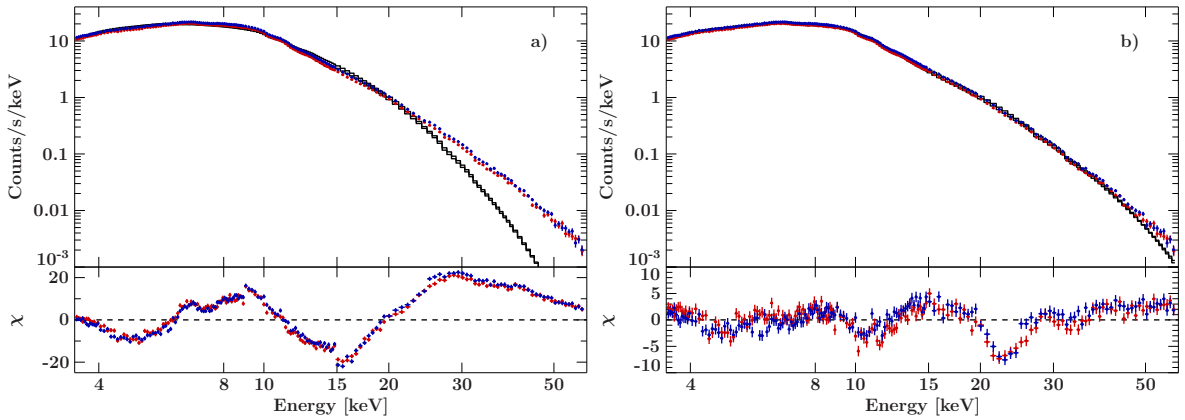

Figure 5: a) Fit of the M1 spectrum with a simple `cutoffpl` model without any further modification. Red data points correspond to data from FPMA and the blue ones to FPMB, respectively. b) Same spectrum as shown in a) but with additional Fe Kα line, 10 keV-feature and ISM absorption. The residuals clearly show the fundamental and first harmonic CRSF.

The residual panel in Figure 5 b shows that the absorbed cutoff powerlaw model, with the Fe Kα emission line and the 10 keV-feature provides a good description of the broadband spectrum, but strong residuals remain at the energies of the CRSFs and the overall fit quality is not acceptable. Therefore further components have to be added.
To model the CRSFs, three multiplicative Gaussian absorption lines of the form

$$M(E) = \exp\left(-\frac{\tau}{\sqrt{2\pi}\sigma}\right) \cdot \exp\left(-\frac{1}{2}\left(\frac{E-E_1}{\sigma}\right)^2\right),$$

were included in the fit function, where E_1, σ, and τ are the line energy, width, and depth. Following the common convention the CRSFs will be labeled with the respective number, starting from 0 for the fundamental line.
The best fit was achieved using three absorption lines at energies of 11 keV, 23 keV, and 34 keV. A particular problem in modeling the 4U 0115+63 spectrum is an artificial parameter correlation between the fundamental CRSF and the 10 keV-feature. Both components are close to each other in energy and one is an emission, the other an absorption component, which can compensate for each other, especially if the powerlaw continuum is left free during the fit. For this reason, "unattended" fits can sometimes lead to unreasonable parameters. This problem is discussed in detail in a forthcoming publication by Kühnel et al. In the case of the observation $M1$ the width of the second harmonic and the energy of the fundamental CRSF had to be fixed to 5 keV and 11.14 keV, respectively, to avoid that the CRSF components model large parts of the continuum. This approach resulted in a reduced χ^2 of 1.48 for observation $M1$ and 1.53 for $M2$.
The best fit parameters for both observations are listed in Table 1, while the resulting fit and residuals are shown in Figure 6 for $M1$ and Figure 18 for $M2$.

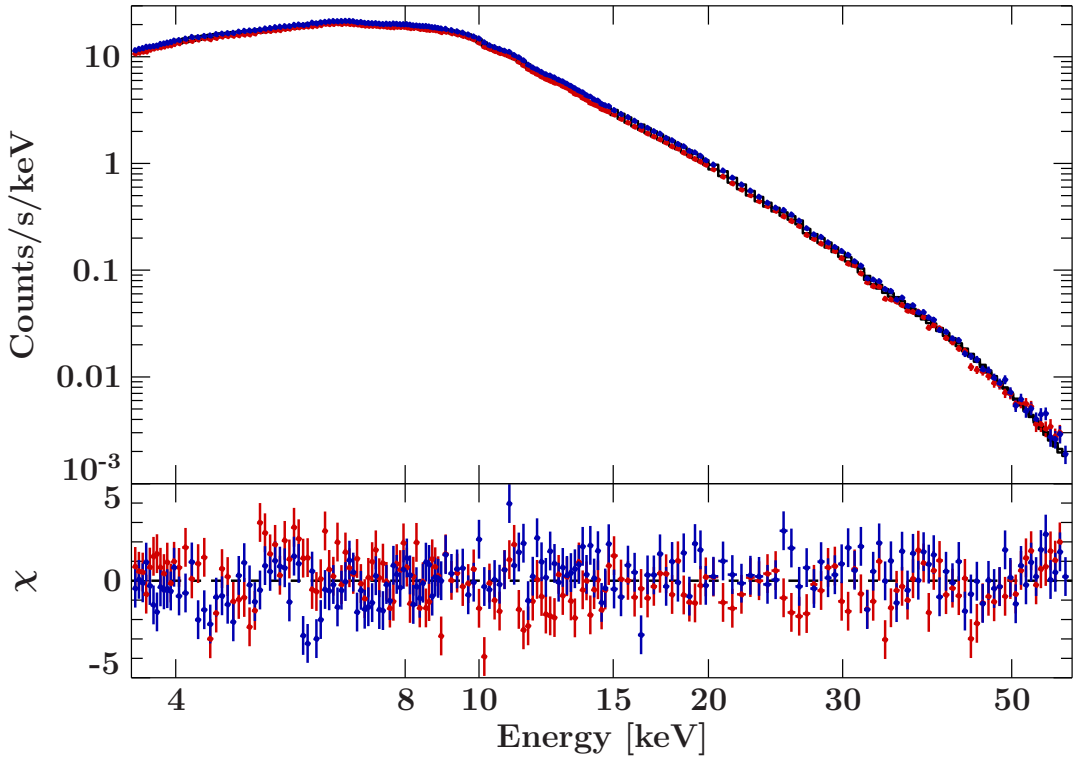

Figure 6: Best fit of the spectrum of observation $M1$.

3.2. Determination of the peak frequencies

Beside its 3.61 s pulse period and orbital modulation 4U 0115+63 is known to show strong, quasi-periodic variability (Heindl et al., 1999). Figure 7 shows the light curve of observation M1 with a time resolution of 3.61 s. The approximate 600 s QPO is clearly visible.

To characterize the spectral variability over the QPO cycle, I first determined the times where the peaks in the light curve reach their maxima. The reason for this was that the peak times are not strictly periodic but the time differences between a peak and its consecutive peak are necessary for the QPO phase definition. The number of all peaks independent of their height in $M1$ is less than 60 and for $M2$ even less than 30, including double peaks and peaks that are not fully observed. In a second step the times were selected manually. Writing a program to automate the selection process would not have simplified the procedure, considering the irregularity of the light curve, the different peak heights, flaring, and missing pulses. One way to improve the selection of the peaks is to rebin the light curve to an integer multiple of the pulse period of 3.61 s and by applying the Savitzky-Golay-smoothing algorithm (Press et al., 1992), a mathematical smoothing filter, to reduce the noise of the signal. This is achieved by fitting a polynomial of the 3rd order using 25 data points to the left and the right of each bin to determine the smoothed curve. Illustrations of the different processing steps are shown in Figure 8.

For the peak time determination, only isolated, single peaks were considered, where maximum was covered by the observation.

Table 1: Best fit parameters of both measurements, with uncertainties given at 90% confidence level.

Parameter	Unit	$M1$	$M2$
N_{H}	10^{22} cm^{-2}	$1.5^{\dagger}$	$1.5^{\dagger}$
c_{FPMA}		$1^{\dagger}$	$1^{\dagger}$
c_{FPMB}		$1.0055^{+0.0016}_{-0.0016}$	$0.9944^{+0.0016}_{-0.0016}$
$E_{\mathrm{CRSF,0}}$	keV	$11.14233^{\dagger}$	$11.59^{+0.15}_{-0.16}$
$\sigma_{\mathrm{CRSF,0}}$	keV	$1.97^{+0.52}_{-0.26}$	$1.91^{+0.30}_{-0.23}$
$\tau_{\mathrm{CRSF,0}}$	keV	$0.77^{+1.41}_{-0.30}$	$0.79^{+0.55}_{-0.27}$
$E_{\mathrm{CRSF,1}}$	keV	$23.36^{+0.22}_{-0.21}$	$23.35^{+0.20}_{-0.20}$
$\sigma_{\mathrm{CRSF,1}}$	keV	$2.08^{+0.24}_{-0.23}$	$2.2^{+0.5}_{-0.4}$
$\tau_{\mathrm{CRSF,1}}$	keV	$0.72^{+0.11}_{-0.11}$	$0.74^{+0.24}_{-0.17}$
$E_{\mathrm{CRSF,2}}$	keV	$34.4^{+0.9}_{-0.9}$	$34.9^{+0.4}_{-0.4}$
$\sigma_{\mathrm{CRSF,2}}$	keV	$5^{\dagger}$	$1.7^{+0.5}_{-0.4}$
$\tau_{\mathrm{CRSF,2}}$	keV	$1.8^{+0.4}_{-0.4}$	$0.71^{+0.20}_{-0.17}$
$F_{\mathrm{PL}}{}^{a}$	keV s^{-1} cm^{-2}	$5.865^{+0.019}_{-0.019}$	$8.57^{+0.4}_{-0.4}$
E_{fold}	keV	$9.43^{+0.14}_{-0.12}$	$9.40^{+0.17}_{-0.17}$
Γ		$0.466^{+0.020}_{-0.017}$	$0.476^{+0.027}_{-0.029}$
$F_{10\,\mathrm{keV}}{}^{a}$	keV s^{-1} cm^{-2}	$1.628^{+0.018}_{-0.018}$	$2.25^{+0.4}_{-0.4}$
$E_{10\,\mathrm{keV}}$	keV	$8.56^{+0.43}_{-0.19}$	$8.58^{+0.33}_{-0.26}$
$\sigma_{10\,\mathrm{keV}}$	keV	$2.83^{+0.06}_{-0.09}$	$3.10^{+0.14}_{-0.15}$
$E_{\mathrm{FeK}\alpha}$	keV	$6.47^{+0.04}_{-0.04}$	$6.42^{+0.05}_{-0.06}$
$\sigma_{\mathrm{FeK}\alpha}$	keV	$0.36^{+0.07}_{-0.07}$	$0.54^{+0.09}_{-0.08}$
$\chi^2_{\mathrm{red/dof}}$		1.48 / 338	1.53 / 338

Notes. $^{(a)}$ Unabsorbed flux in the energy band from 3 to 50 keV, unit [keV s^{-1} cm^{-2}].
$^{(\dagger)}$ Fixed parameter.

The times of all peaks that could be clearly identified in the rebinned and smoothed light curve considering these criteria are listed in Table 4 for observation $M1$ and in Table 5 for $M2$. Using these results, Figure 9 shows the time differences between consecutive peaks as a function of the peak number. For further reference, all peak arrival times for both observations are listed in the appendix (Table 4 and Table 5). The times between pulses scatter between ∼300 s and ∼800 s. This distribution is also shown in Figure 10. Although the histogram of the peak arrival times is limited by the low number of data points (less than 30 peaks in $M1$ and less than 15 in $M2$), it indicates a bimodal distribution rather than a single peak around the estimated QPO

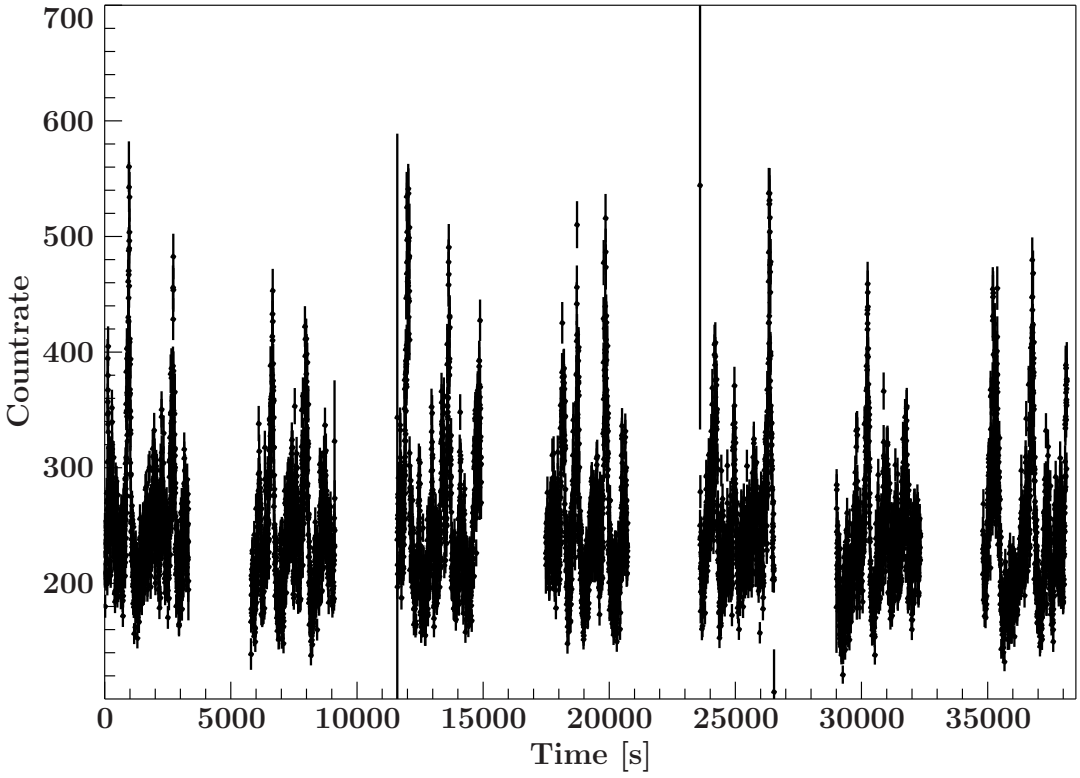

Figure 7: The entire light curve of $M1$, measured with the detector FPMA. The observation spans roughly 40 ks. Gaps in the light curve are caused by the satellite orbit and screening criteria and result in the net exposure of 15 ks.

period. Probably, individual, weak peaks could not be identified, leading to an overestimation of the QPO period. The peak morphology is also often asymmetric and irregular flaring of the light curve makes a clear distinction of many of the peaks very difficult. For all of these reasons, a unique QPO phase definition only based on the peak arrival times was not possible.

3.3. Hardness Ratio

In order to investigate the spectral variability independent of the QPO phase definition, I calculated hardness ratios for three energy bands and compared their time evolution with the observed count rate. Hardness ratios are calculated by dividing the count rate or flux of one energy band by the count rate or flux of another energy band and therefore provide a direct and model-independent measure of changes of the spectral shape. Hardness ratios are mostly used to analyse observations from faint sources that provide a restricted number of events. Therefore they are a common evaluation technique in high-energy astrophysics and are often used to give a rough overview of the spectral properties. The two definitions commonly used in the literature are dividing the count rate in the two energy bands a and b (e.g., Jin et al., 2006; Park et al., 2006), i.e.,

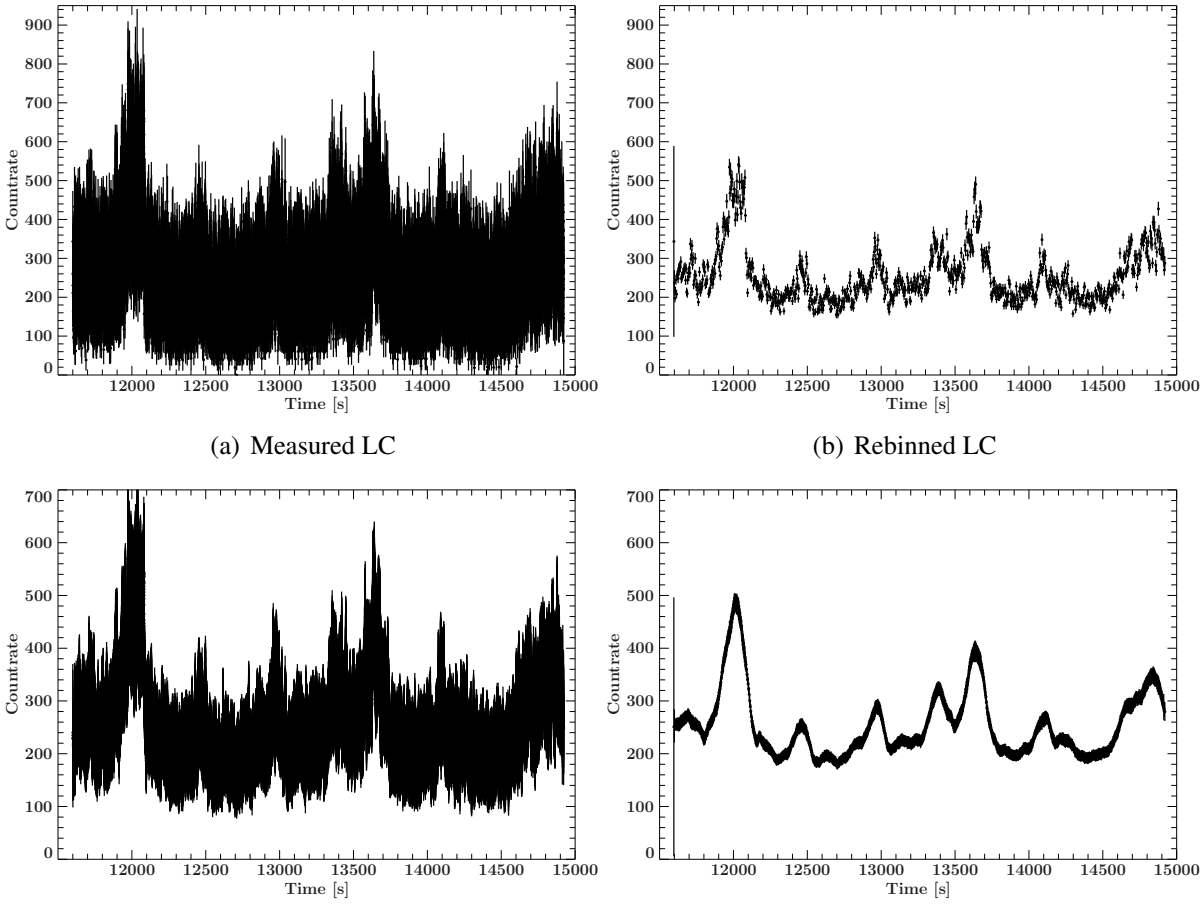

(a) Measured LC

(b) Rebinned LC

(c) Smoothed LC

(d) Smoothed and rebinned LC

Figure 8: (a) Light curve of observation $M1$ from 11500 s to 15 000 s with a bin size of 0.1 s. (b) and (d) rebinned light curve with a binsize of 3.61 s. (c) and (d) show the original and rebinned light curve after applying the Savitzky-Golay-smooting, using a polynomial of 3rd order, while taking 25 data points to the left and the right into account.

$$\mathrm{HR}_1 = \frac{b}{a},$$

or taking the ratio between the difference and the sum of the count rates

$$\mathrm{HR}_2 = \frac{b-a}{b+a}.$$

In contrast to Roy et al. (2019), who analysed hardness ratios of 4U 0115+63 of the 3–8 keV and 15–30 keV band taken with LAXPC/AstroSat, I divided the NuSTAR observations $M1$ and $M2$ into three energy bands, 4 keV to 7 keV, 7 keV to 15 keV, and a high energetic part from 15 keV to 50 keV, to particularly track any variability around the 10 keV-feature and the fundamental CRSF.

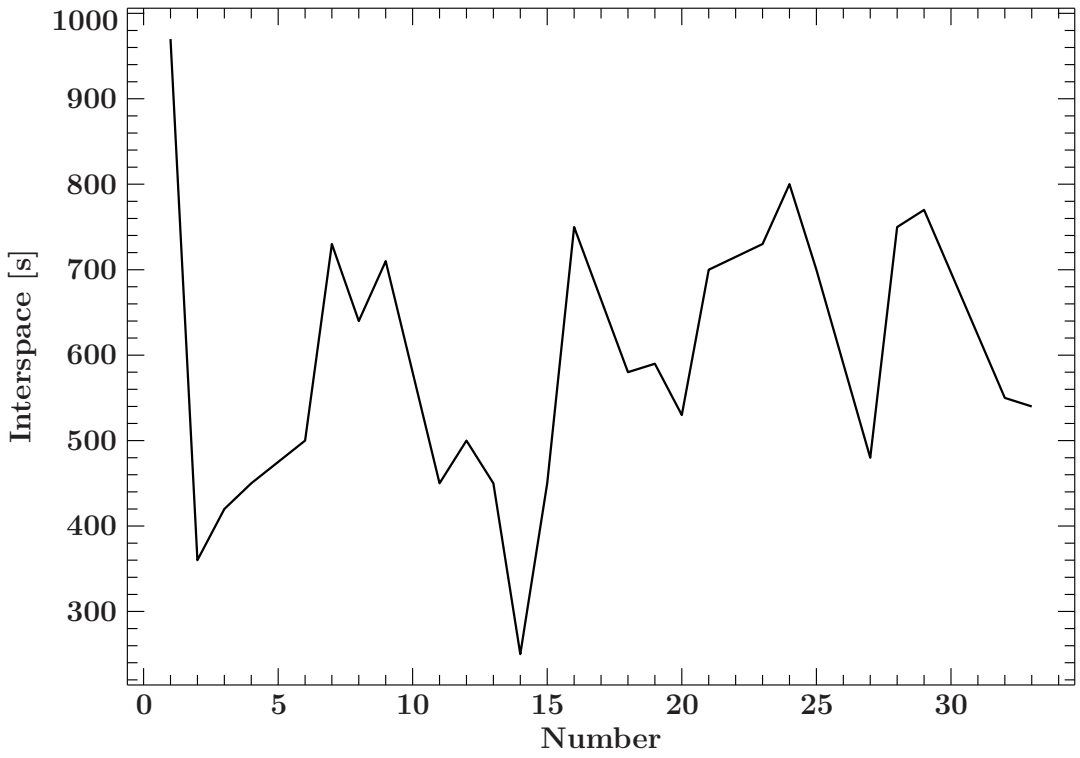

Figure 9: Time differences between consecutive peaks in observation $M1$ as a function of the peak number. Peaks have only been considered consecutive in segments of the light curve that had no gaps greater than 1000 s.

The following evaluation was performed with the default settings of the ISIS function `hardnessratio`, which uses the first definition of hardness rations, HR_1. Uncertainties of the hardness ratios have been calculated by propagating the uncertainties of the count rates. Out of the different energy bands three hardness ratios were determined for each segment of the light curve, using the low and medium energies for the hardness ratio HR12, the low and high energetic bands for HR13 and the medium and high energy band for HR23. A segment of the light curve from $M1$ with the three associated hardness ratios is shown in Figure 11. The other parts of the light curve and $M2$ were evaluated in the same way. Another example is displayed in Figure 21 in the appendix.
Examining the hardness ratios and comparing their variability to the light curve itself, it appears that the hardness ratios HR12 and HR23 change most significantly during strong peaks in the light curve, but remain rather constant during weak peaks, off-peaks, and slight flaring. This variability is less significant in HR13. This behavior is similar in both observations $M1$ and $M2$. This result leads to the conclusion that the spectral variability with the QPO is most prominent when a strong peak shows up in the light curve and that mostly the energy range from 7 keV to 15 keV contributes to the observed spectral variability. Based on these results I extracted spectra during the rise and decay of the peaks and off-peak times to investigate the nature of this variability in more detail.

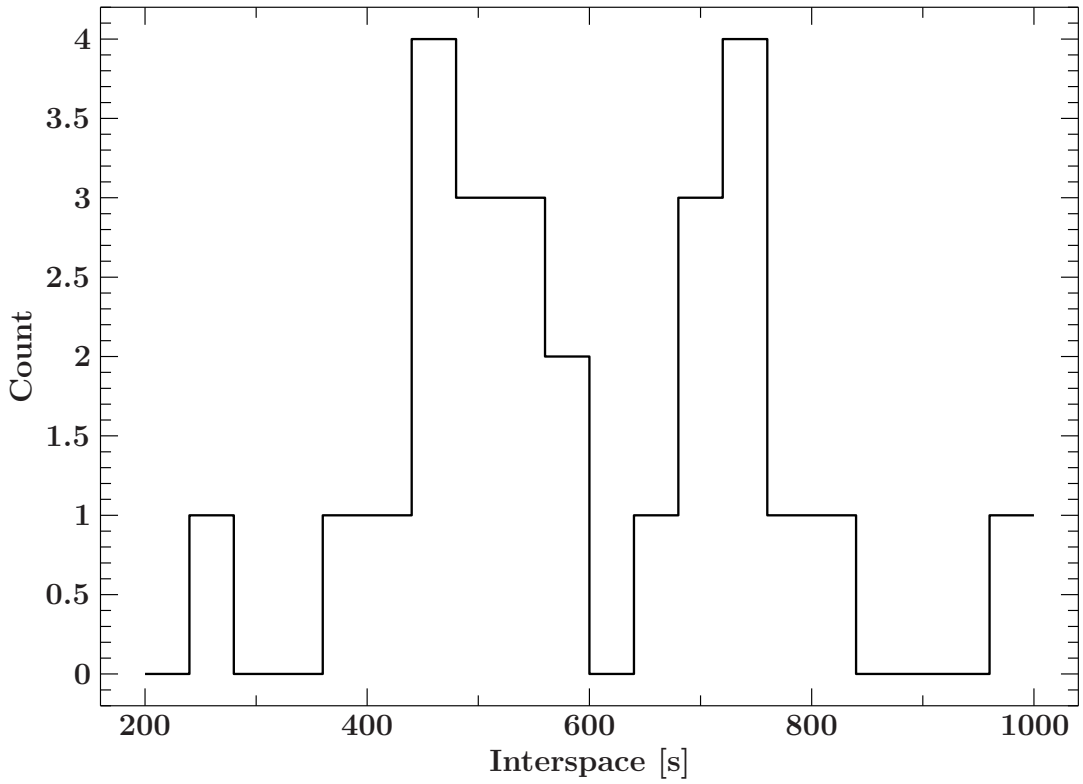

Figure 10: Histogram showing the distribution of the time interspaces between the selected peaks from observation $M1$.

3.4. Time-resolved spectroscopy

Analog to the analyses in subsection 3.2, where the times when a peak reached its maximum were determined, the start and stop times of the increasing and decreasing slope of the peaks were determined from the light curve. The slopes were first considered separately, because they can be easily combined together to take the whole peak into account if need be. An example of this selection for $M1$ is shown in Figure 12, where the blue-shaded regions mark the time intervals chosen for the extraction of the time-resolved spectra. Another sample, using the light curve of $M2$, is shown in Figure 22 in the Appendix.
Good Time Intervals (GTI) files were created from the time intervals described above after conversion to the NuSTAR reference time system which is seconds since MJD 55197.00076601852. These can be passed directly to the NuSTAR extraction pipeline to extract time-resolved spectra applying all screening and calibration criteria mentioned in the previous sections.
For illustration, Figure 13 and Figure 14 show the evaluation of the best fit model of the time-averaged spectrum (after re-scaling) on the increasing and decreasing slope, whole peak and off-peak spectra for observation $M1$. The corresponding residuals show that the time-resolved spectra only differ locally from the time averaged spectrum around 10 keV. In particular, the off-peak spectrum shows an excess around ~10 keV, whereas the peak spectrum dips at this energy. This is to be expected, because the sum of both results again in the time-averaged spectrum.

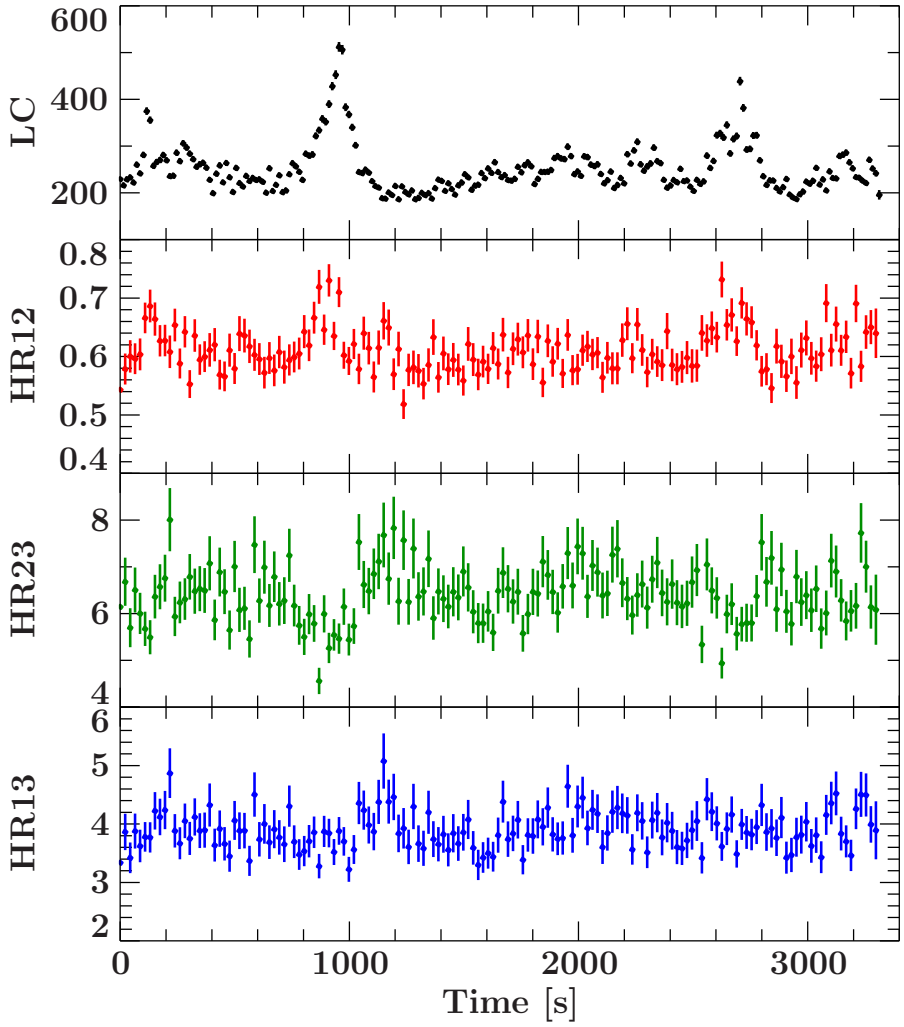

Figure 11: Light curve and hardness ratios of $M1$ in the range from 0 to 3400 s with respect to the start of the observation. The spectrum was divided into three energy bands, from 4 keV to 7 keV, 7 keV to 15 keV, and 15 keV to 50 keV. HR12 was calculated using the soft and medium energy band, HR13 contains information of the soft and hard band and HR23 combined the medium and hard band.

There are two features located in this energy region, the 10 keV-feature and the fundamental CRSF. Assuming that the spectral change originates from a variation of the CRSFs, the harmonic absorption lines should also vary to some extent, resulting in further deviations at higher energies, which is not the case. Therefore, it is very likely that the spectral change originates in a variation of the 10 keV-feature. To test this assumption the CRSF parameters were fixed and the model was fitted again to check whether the spectral change can only be accounted for by the changes of the 10 keV-feature and the powerlaw continuum. The best fit parameters for observation $M1$ are listed in Table 2, those for $M2$ are listed in appendix Table 8.
In Figure 15 it can be seen that after re-fitting the model describes the data very accurately.

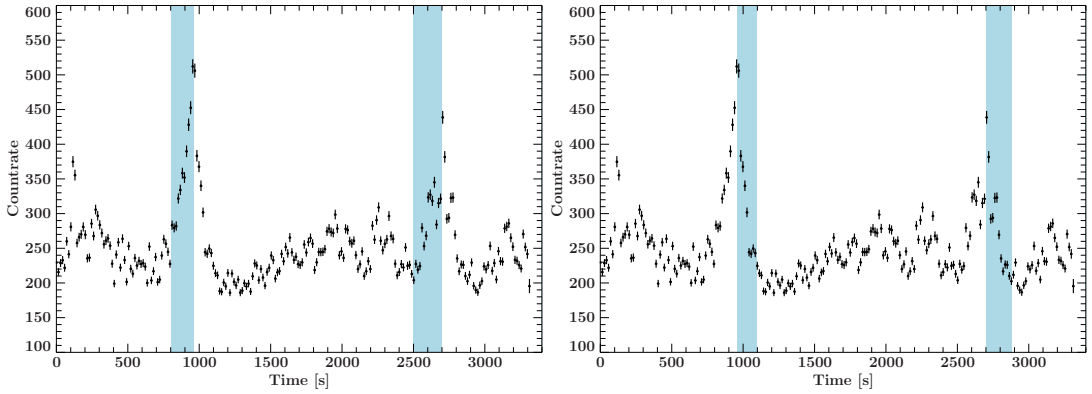

(a) Increasing slope (b) Decreasing slope

Figure 12: Section of the light curve of $M1$, from 0 s to 3400 s. The blue shaded regions show the segments that were selected for further analysis.

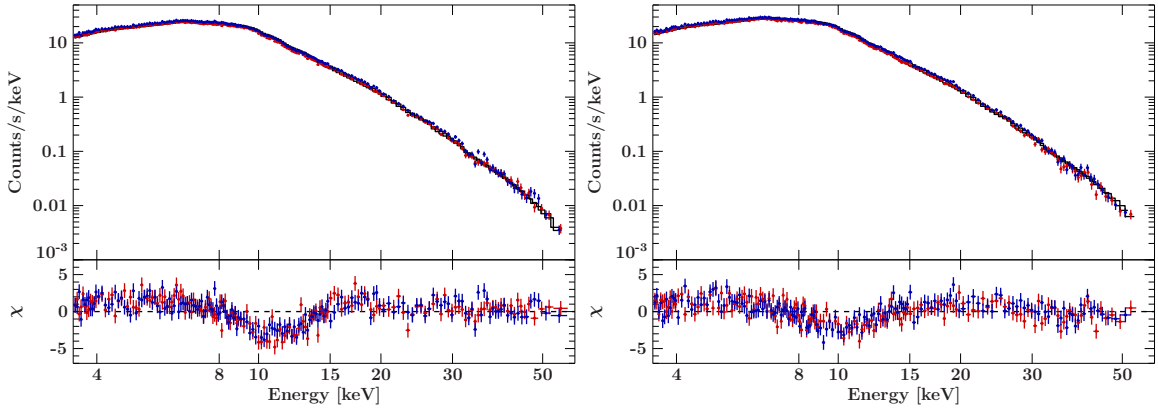

(a) Increasing slope (b) Decreasing slope

Figure 13: Spectra of the (a) increasing and (b) decreasing slope of the peaks observed in the light curve of $M1$.

Comparing the best-fit parameters of the time-resolved spectra to those of the time-averaged spectrum, I find that the photon index and folding energy only change marginally between the peak and off-peak spectra and are obviously close to the time-averaged spectrum. Fluxes of the powerlaw and 10 keV-feature roughly scale with the count rate during peak and off-peak. The width of the 10 keV-feature does not change between the peak and off-peak spectrum and its energy only is slightly higher during the off-peak. A similar behavior was observed in observation $M2$, although less distinct than for measurement $M1$. The residual panels, shown in Figure 14, indicate that most of the spectral variability between peak and off-peak is caused by the 10 keV-feature, so of particular interest is its flux related to the flux of the powerlaw continuum. Table 3 therefore lists the flux ratios of these two components. The flux ratios during peak and off-peak vary up to ∼15% and ∼5%, respectively, with respect to the observation-averaged spectrum.

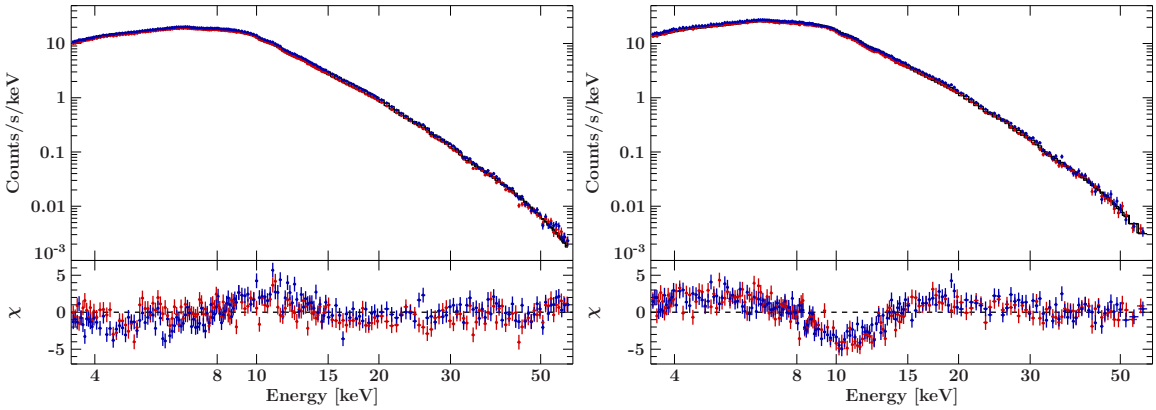

(a) Off-peak (b) Peak

Figure 14: Spectra of the (a) off-peak and (b) peak part of the observed light curve of $M1$, compared to the best fit continuum derived from the time-averaged spectrum.

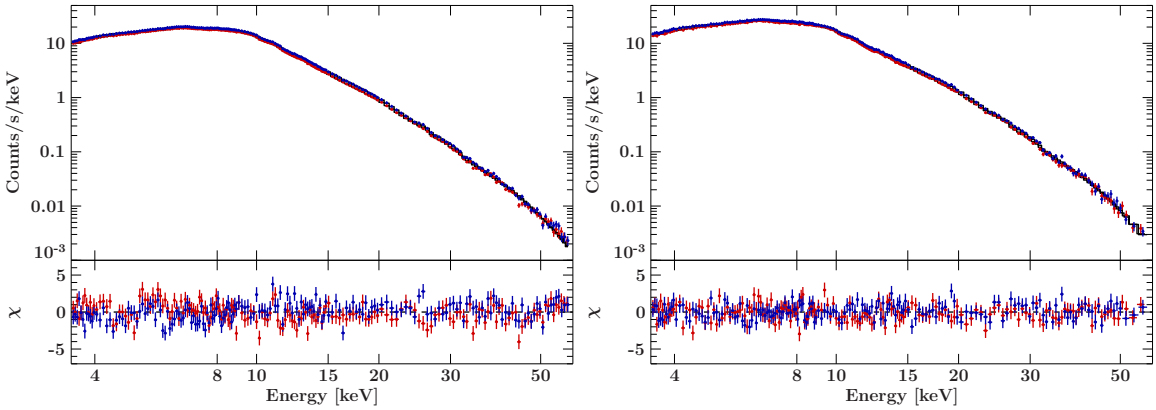

(a) Off-peak (b) Peak

Figure 15: The figures show the re-fitted spectra of the (a) off-peak and (b) peak states of the observed light curve of $M1$.

Table 2: Best fit parameters of observation $M1$ considering different parts of the spectrum, with uncertainties given at 90% confidence level.

Parameter	increasing	decreasing	peak	off-peak	time-averaged
$N_{\rm H}$ [10^{22} cm^{-2}]	$1.5^{\dagger}$	$1.5^{\dagger}$	$1.5^{\dagger}$	$1.5^{\dagger}$	$1.5^{\dagger}$
$c_{\rm FPMA}$	$1^{\dagger}$	$1^{\dagger}$	$1^{\dagger}$	$1^{\dagger}$	$1^{\dagger}$
$c_{\rm FPMB}$	$1.0055^{\dagger}$	$1.0055^{\dagger}$	$1.0055^{\dagger}$	$1.0055^{\dagger}$	$1.0055^{\dagger}$
$E_{\rm CRSF,0}$ [keV]	$11.14233^{\dagger}$	$11.14233^{\dagger}$	$11.14233^{\dagger}$	$11.14233^{\dagger}$	$11.14233^{\dagger}$
$\sigma_{\rm CRSF,0}$ [keV]	$1.97^{\dagger}$	$1.97^{\dagger}$	$1.97^{\dagger}$	$1.97^{\dagger}$	$1.97^{\dagger}$
$\tau_{\rm CRSF,0}$ [keV]	$0.77^{\dagger}$	$0.77^{\dagger}$	$0.77^{\dagger}$	$0.77^{\dagger}$	$0.77^{\dagger}$
$E_{\rm CRSF,1}$ [keV]	$23.36^{\dagger}$	$23.36^{\dagger}$	$23.36^{\dagger}$	$23.36^{\dagger}$	$23.36^{\dagger}$
$\sigma_{\rm CRSF,1}$ [keV]	$2.08^{\dagger}$	$2.08^{\dagger}$	$2.08^{\dagger}$	$2.08^{\dagger}$	$2.08^{\dagger}$
$\tau_{\rm CRSF,1}$ [keV]	$0.72^{\dagger}$	$0.72^{\dagger}$	$0.72^{\dagger}$	$0.72^{\dagger}$	$0.72^{\dagger}$
$E_{\rm CRSF,2}$ [keV]	$34.4^{\dagger}$	$34.4^{\dagger}$	$34.4^{\dagger}$	$34.4^{\dagger}$	$34.4^{\dagger}$
$\sigma_{\rm CRSF,2}$ [keV]	$5^{\dagger}$	$5^{\dagger}$	$5^{\dagger}$	$5^{\dagger}$	$5^{\dagger}$
$\tau_{\rm CRSF,2}$ [keV]	$1.8^{\dagger}$	$1.8^{\dagger}$	$1.8^{\dagger}$	$1.8^{\dagger}$	$1.8^{\dagger}$
$F_{\rm PL}{}^{a}$	$7.11^{+0.07}_{-0.07}$	$8.14^{+0.09}_{-0.09}$	$7.55^{+0.06}_{-0.06}$	$5.484^{+0.020}_{-0.021}$	$5.865^{+0.019}_{-0.019}$
$E_{\rm fold}$ [keV]	$9.15^{+0.21}_{-0.21}$	$8.94^{+0.22}_{-0.21}$	$9.11^{+0.15}_{-0.15}$	$9.49^{+0.10}_{-0.10}$	$9.43^{+0.08}_{-0.08}$
Γ	$0.422^{+0.027}_{-0.027}$	$0.408^{+0.029}_{-0.029}$	$0.422^{+0.020}_{-0.020}$	$0.475^{+0.011}_{-0.011}$	$0.466^{+0.010}_{-0.010}$
$F_{10\,\rm keV}{}^{a}$	$1.65^{+0.07}_{-0.07}$	$1.91^{+0.08}_{-0.08}$	$1.78^{+0.05}_{-0.05}$	$1.591^{+0.019}_{-0.019}$	$1.628^{+0.018}_{-0.018}$
$E_{10\,\rm keV}$ [keV]	$8.23^{+0.08}_{-0.09}$	$8.35^{+0.09}_{-0.09}$	$8.28^{+0.06}_{-0.07}$	$8.642^{+0.024}_{-0.024}$	$8.56^{+0.023}_{-0.023}$
$\sigma_{10\,\rm keV}$ [keV]	$2.80^{+0.08}_{-0.08}$	$2.87^{+0.08}_{-0.08}$	$2.84^{+0.06}_{-0.06}$	$2.820^{+0.023}_{-0.023}$	$2.83^{+0.021}_{-0.021}$
$E_{\rm FeK\alpha}$ [keV]	$6.47^{\dagger}$	$6.47^{\dagger}$	$6.47^{\dagger}$	$6.47^{\dagger}$	$6.47^{\dagger}$
$\sigma_{\rm FeK\alpha}$ [keV]	$0.36^{\dagger}$	$0.36^{\dagger}$	$0.36^{\dagger}$	$0.36^{\dagger}$	$0.36^{\dagger}$
$\chi^2_{\rm red/dof}$	1.03 / 337	1.04 / 336	1.05 / 350	1.51 / 364	1.48 / 338

Notes. $^{(a)}$ Unabsorbed flux in the energy band from 3 to 50 keV, unit [keV s^{-1} cm^{-2}].
$^{(\dagger)}$ Fixed parameter.

Table 3: Ratios between the unabsorbed 3–50 keV fluxes of the powerlaw continuum and the 10 keV-feature in observation *M*1. The fluxes have the unit [keV s^{-1} cm^{-2}].

	Flux PL	Flux 10 keV	Quotient
total	$5.865^{+0.019}_{-0.019}$	$1.628^{+0.018}_{-0.018}$	$0.278^{+0.004}_{-0.004}$
increasing	$7.11^{+0.07}_{-0.07}$	$1.65^{+0.07}_{-0.07}$	$0.232^{+0.011}_{-0.011}$
decreasing	$8.14^{+0.09}_{-0.09}$	$1.91^{+0.08}_{-0.08}$	$0.235^{+0.011}_{-0.011}$
peak	$7.55^{+0.06}_{-0.06}$	$1.78^{+0.05}_{-0.05}$	$0.235^{+0.007}_{-0.007}$
off-peak	$5.484^{+0.020}_{-0.021}$	$1.591^{+0.019}_{-0.019}$	$0.290^{+0.004}_{-0.004}$

4. Summary and Discussion

In this thesis I analyzed two NuSTAR observations of the BeXRB 4U 0115+63 taken at the peak and during the decay phase of its 2015 outburst. The broad-band spectrum of both observations is well described by an empirical powerlaw model with exponential cutoff, modified by interstellar absorption and a broad Fe Kα emission line, possibly indicating higher ionization states of iron. The fundamental CRSF around 11 keV and two harmonics could be clearly identified in both observations. The continuum model further requires an emission component around ~8.5 keV, commonly known as the 10 keV-feature. The presence of this feature in the spectrum of 4U 0115+63 has first been reported by (Coburn, 2001). The choice of the continuum model was motivated by its successful application in previous analyses and because it was shown to minimize systematic effects on the CRSF modeling (Müller et al., 2013). The NuSTAR observations do not confirm the existence of two fundamental CRSFs at ~11 keV and ~15 keV, as suggested by Iyer et al. (2015).

The light curve shows strong variability related to a known ~600 s QPO that was already discovered by RXTE (Heindl et al., 1999). The main focus of this work was to characterize the spectral variability associated with this QPO. Investigating the distribution of the pulse arrival times, the morphology of the light curve showed that a clear definition of the QPO phase was not possible. Motivated by the variability of the hardness ratios with time, time-resolved spectra were extracted for the rise and decay phases of the QPO peaks, as well as the off-peak times. Fitting these spectra with the model used for the time-averaged spectrum showed that most of the spectral variabilities can be accounted for by changes of the 10 keV-feature component, which varies up to ~20% in flux compared to the powerlaw continuum between peaks and off-peaks.

The nature of the 10 keV-feature and the QPO are both still under debate. Ferrigno et al. (2009) proposed Comptonized cyclotron emission as the origin of the 10 keV-feature. According to Becker & Wolff (2007), the Comptonization of bremsstrahlung produced by the decelerating plasma is the main contribution to the powerlaw-like continuum. Although the origin of the QPO is not well understood, its effect is a change of the luminosity and therefore probably mass accretion rate by ~50% on timescales of a few hundred seconds. The different variability of the powerlaw and 10 keV-feature flux might indicate that these two emission processes react differently to sudden changes of the mass accretion rate.

Starting from this assumption a next step would be to perform flux-resolved spectroscopy, which can also resolve the irregular or flaring parts of the light curve. Furthermore, the relation between the powerlaw and the 10 keV-feature flux could also be studied during an outburst of the source, where the luminosity can vary by more than an order of magnitude, although the timescale is clearly different. Future analyses will also have to critically test the assumption that the CSRFs do not change with QPO phase, which was necessary for avoiding parameter degeneracies in the fit, but would introduce strong systematic effects if incorrect. Finally, the excellent time resolution of the NuSTAR data will also allow dedicated pulse phase-resolved spectroscopy.

A. Appendix

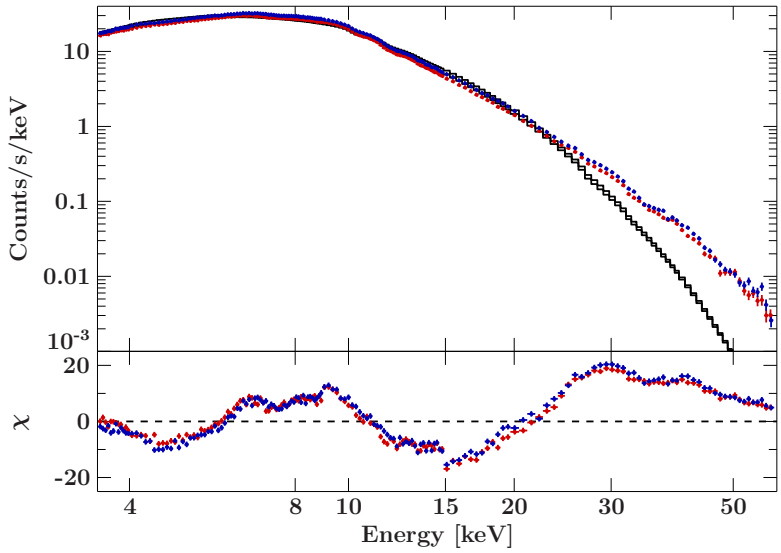

Figure 16: Fit of the M2 spectrum with a simple cutoff powerlaw model without any further modification. Red data points correspond to data from FPMA and the blue ones to FPMB, respectively.

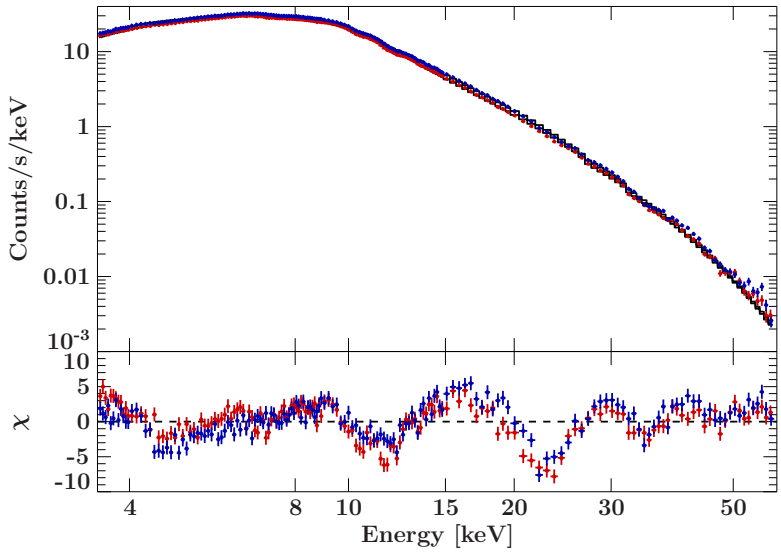

Figure 17: Fit of the *M*2 spectrum using a simple cutoff powerlaw with additional Fe Kα line, 10 keV-feature and ISM absorption. The red points correspond to data from FPMA, the blue ones from FPMB, respectively. The residuals clearly show the fundamental and first harmonic CRSF.

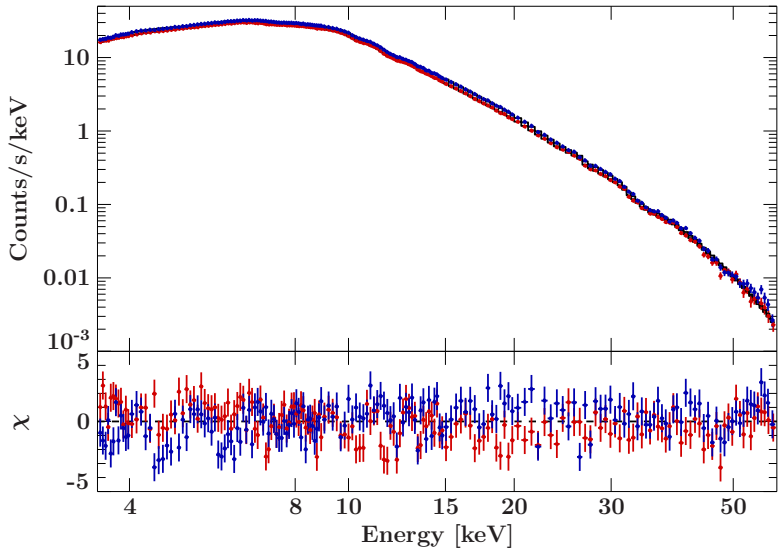

Figure 18: Best fit of the spectrum of observation *M*2.

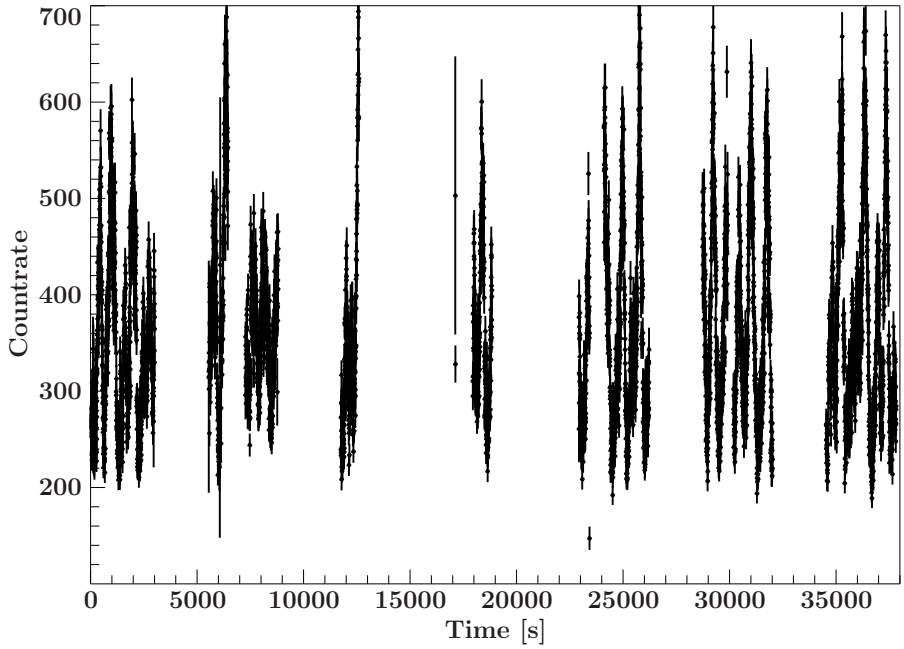

Figure 19: The entire light curve of *M*2, measured with the detector FPMA. The observation spans roughly 40 ks. Gaps in the light curve are caused by the satellite orbit and screening criteria and result in the net exposure of 9 ks.

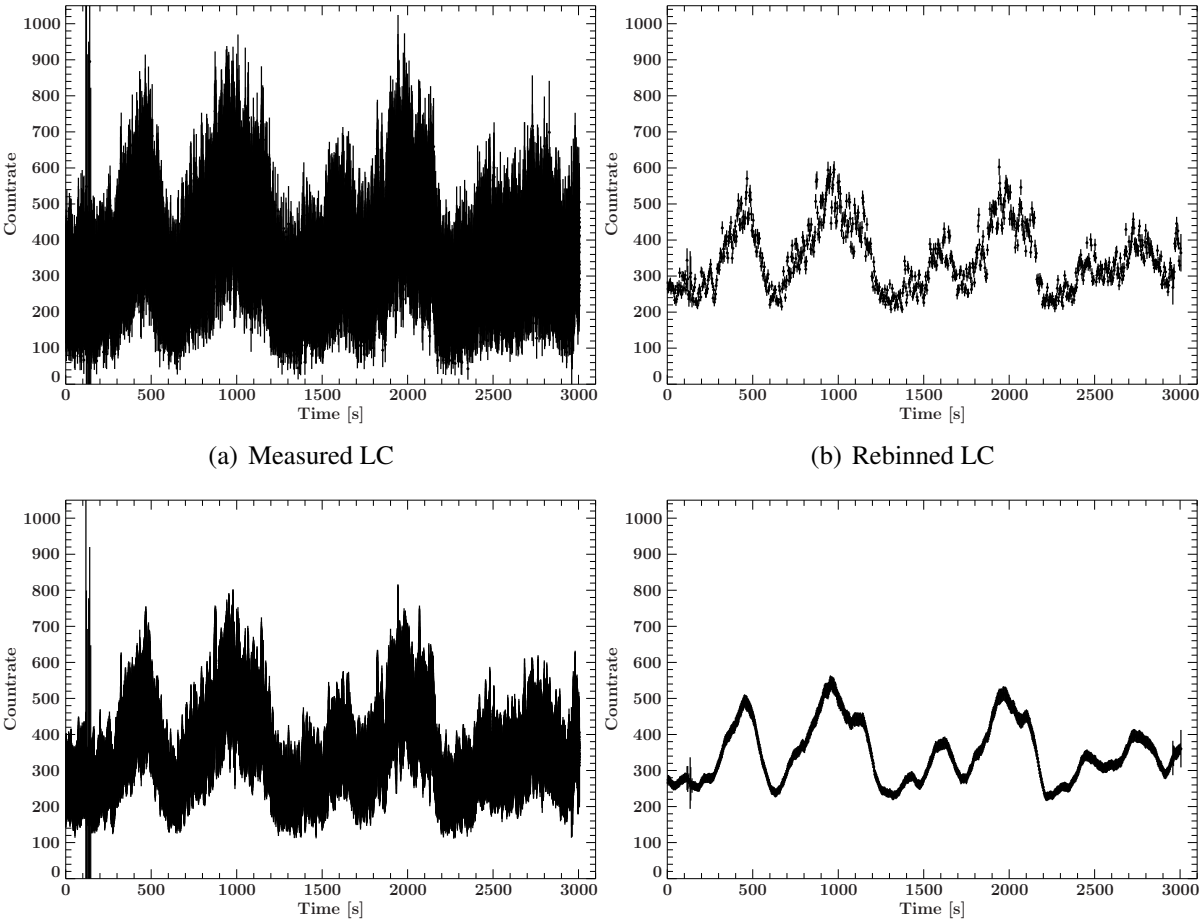

(a) Measured LC

(b) Rebinned LC

(c) Smoothed LC

(d) Smoothed and rebinned LC

Figure 20: (a) Light curve of observation *M*2 from 0 to 3100 s with a bin size of 0.1 s. (b) and (d) rebinned light curve with a bin size of 3.61 s. (c) and (d) show the original and rebinned light curve after applying the Savitzky-Golay-smooting, using a polynomial of 3rd order, while taking 20 data points to the left and the right into account.

Table 4: Times of all selected peaks from observation $M1$. Additionally the duration between a peak and its successive peak is listed.

Peak Nr.	Time t [s]	$t_{i+1} - t_i$
1	950	970
2	1920	360
3	2280	420
4	2700	450
5	3150	2970
6	6120	500
7	6620	730
8	7350	640
9	7990	710
10	8700	3300
11	12000	450
12	12450	500
13	12950	450
14	13400	250
15	13650	450
16	14100	750
17	14850	3300
18	18150	580
19	18730	590
20	19320	530
21	19850	700
22	20550	3670
23	24220	730
24	24950	800
25	25750	700
26	26450	3300
27	29750	480
28	30230	750
29	30980	770
30	31750	3500
31	35250	1550
32	36800	550
33	37350	540
34	37890	-

Table 5: Times of all identified peaks from observation *M2* and the duration between a peak and its successive peak.

Peak Nr.	Time t [s]	$t_{i+1} - t_i$
1	470	490
2	960	670
3	1630	350
4	1980	770
5	2750	3630
6	6380	1770
7	8150	3860
8	12010	5990
9	18000	360
10	18360	5020
11	23380	1600
12	24980	800
13	25780	3450
14	29230	1220
15	30450	550
16	31000	740
17	31740	3540
18	35280	1080
19	36360	580
20	36940	800
21	37740	-

Table 6: Ratios between the unabsorbed 3–50 keV fluxes of the powerlaw continuum and the 10 keV-feature in observation *M2*. The fluxes have the unit [keV s^{-1} cm^{-2}]

	Flux PL	Flux 10 keV	Quotient
total	$8.57^{+0.04}_{-0.04}$	$2.25^{+0.04}_{-0.04}$	$0.263^{+0.005}_{-0.005}$
increasing	$10.04^{+0.07}_{-0.08}$	$2.33^{+0.07}_{-0.07}$	$0.232^{+0.008}_{-0.008}$
decreasing	$9.88^{+0.08}_{-0.08}$	$2.51^{+0.08}_{-0.08}$	$0.254^{+0.009}_{-0.009}$
peak	$10.05^{+0.06}_{-0.06}$	$2.41^{+0.06}_{-0.06}$	$0.240^{+0.007}_{-0.007}$
off-peak	$7.42^{+0.05}_{-0.05}$	$2.13^{+0.04}_{-0.04}$	$0.287^{+0.008}_{-0.008}$

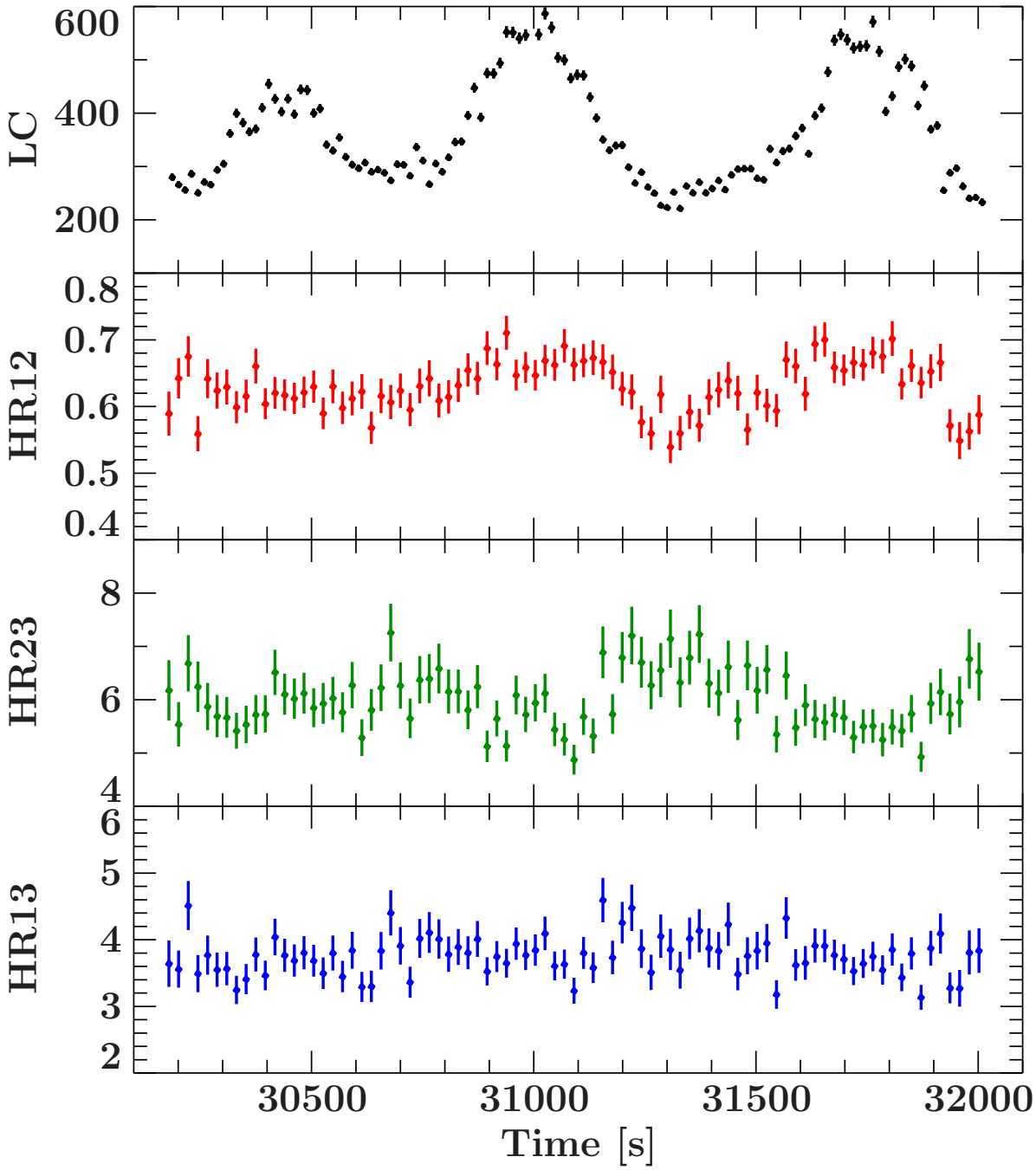

Figure 21: A segment of the light curve of *M*2 is shown from 30100 to 32 100 s. Additionally the relevant hardness ratios are illustrated. The selected energy bands ranged from 4 keV to 7 keV, 7 keV to 15 keV, and 15 keV to 50 keV.

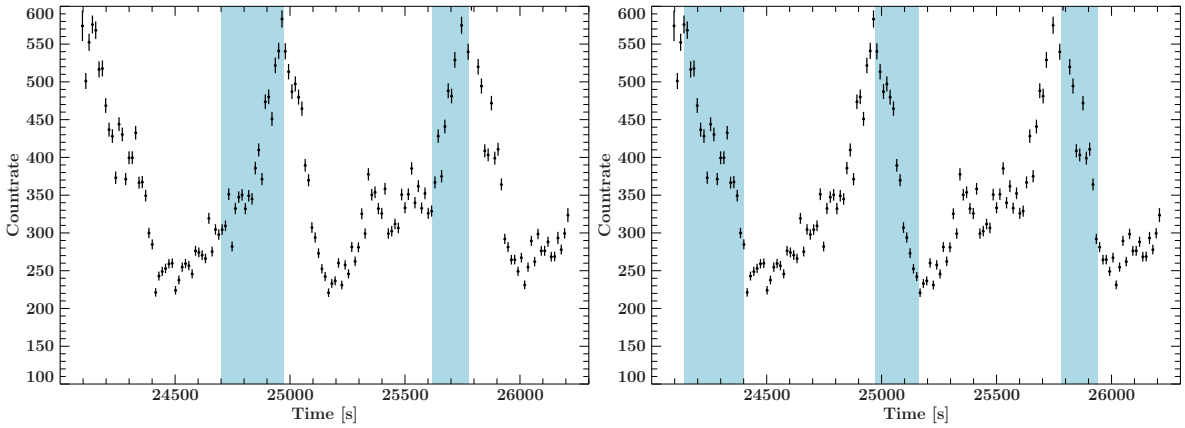

(a) Increasing slope (b) Decreasing slope

Figure 22: Section of the light curve of $M2$, from 24 000 s to 26 300 s. The blue shaded regions show the parts that were selected for further analysis.

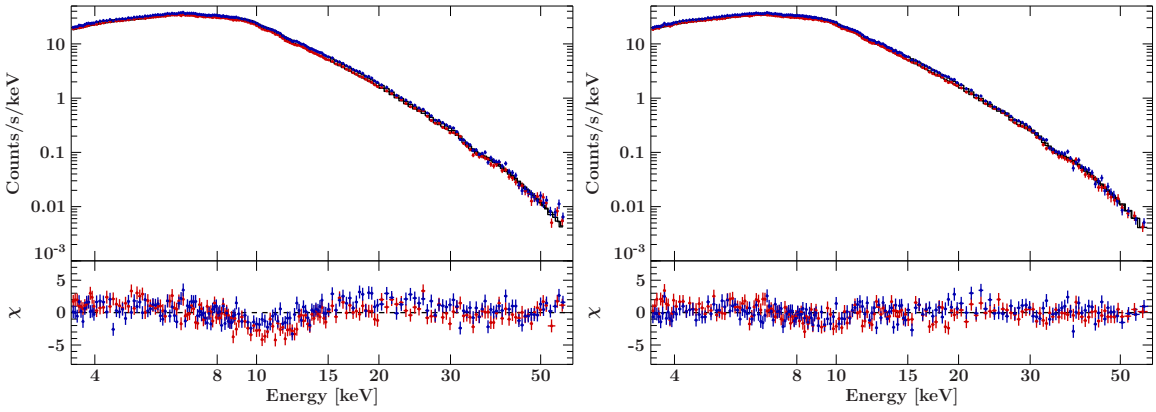

(a) increasing slope (b) decreasing slope

Figure 23: Spectra of the (a) increasing and (b) decreasing slopes of the peaks of the light curve from $M2$. The fit was performed using the best fit parameters, determined by fitting the time-averaged spectra.

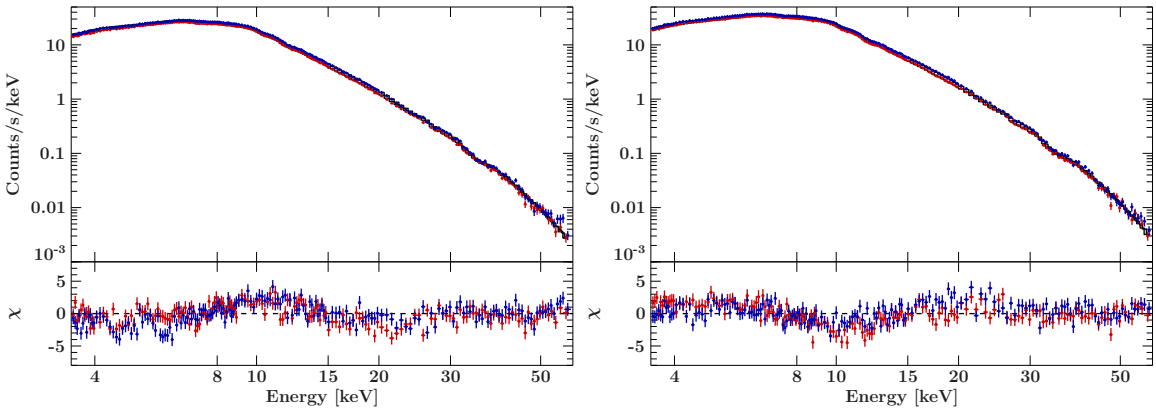

(a) off peak (b) peak

Figure 24: Spectra of the (a) off-peak states and (b) the peaks of the light curve from *M*2. The fit was performed using the best fit parameters, determined by fitting the spectra of the complete light curve.

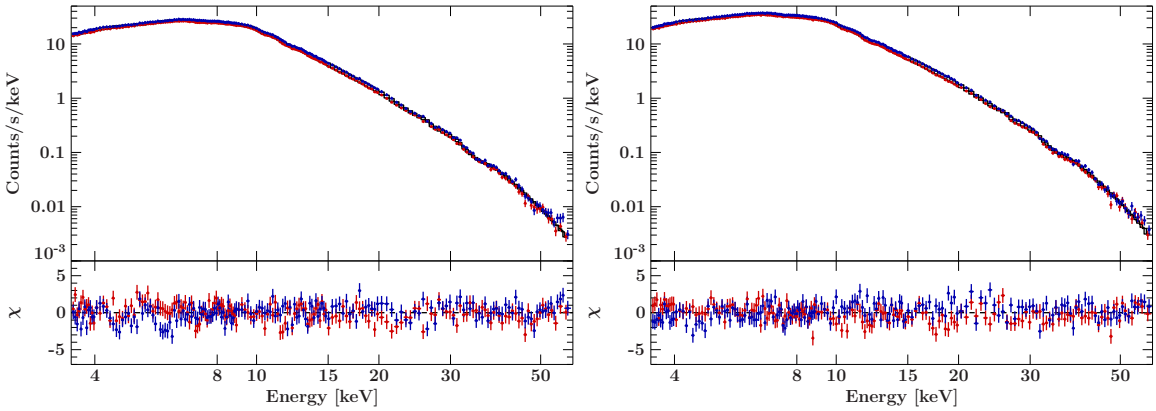

(a) off peak (b) peak

Figure 25: Spectra of the again fitted (a) off-peak states and (b) peaks of the light curve from *M*2.

A.1. Fit parameters

Table 7: Best fit parameters of both measurements, with uncertainties given at 90% confidence level.

Parameter	Unit	$M1$	$M2$
$N_{\rm H}$	10^{22} cm^{-2}	$1.5^{\dagger}$	$1.5^{\dagger}$
$c_{\rm FPMA}$		$1^{\dagger}$	$1^{\dagger}$
$c_{\rm FPMB}$		$1.0055^{+0.0016}_{-0.0016}$	$0.9944^{+0.0016}_{-0.0016}$
$E_{\rm CRSF,0}$	keV	$11.14233^{\dagger}$	$11.59^{+0.15}_{-0.16}$
$\sigma_{\rm CRSF,0}$	keV	$1.97^{+0.52}_{-0.26}$	$1.91^{+0.30}_{-0.23}$
$\tau_{\rm CRSF,0}$	keV	$0.77^{+1.41}_{-0.30}$	$0.79^{+0.55}_{-0.27}$
$E_{\rm CRSF,1}$	keV	$23.36^{+0.22}_{-0.21}$	$23.35^{+0.20}_{-0.20}$
$\sigma_{\rm CRSF,1}$	keV	$2.08^{+0.24}_{-0.23}$	$2.2^{+0.5}_{-0.4}$
$\tau_{\rm CRSF,1}$	keV	$0.72^{+0.11}_{-0.11}$	$0.74^{+0.24}_{-0.17}$
$E_{\rm CRSF,2}$	keV	$34.4^{+0.9}_{-0.9}$	$34.9^{+0.4}_{-0.4}$
$\sigma_{\rm CRSF,2}$	keV	$5^{\dagger}$	$1.7^{+0.5}_{-0.4}$
$\tau_{\rm CRSF,2}$	keV	$1.8^{+0.4}_{-0.4}$	$0.71^{+0.20}_{-0.17}$
$F_{\rm PL}{}^{a}$	keV s^{-1} cm^{-2}	$5.865^{+0.019}_{-0.019}$	$8.57^{+0.04}_{-0.04}$
$E_{\rm fold}$	keV	$9.43^{+0.08}_{-0.08}$	$9.40^{+0.09}_{-0.09}$
Γ		$0.466^{+0.010}_{-0.010}$	$0.476^{+0.011}_{-0.011}$
$F_{10\,\rm keV}{}^{a}$	keV s^{-1} cm^{-2}	$1.628^{+0.018}_{-0.018}$	$2.25^{+0.04}_{-0.04}$
$E_{10\,\rm keV}$	keV	$8.56^{+0.023}_{-0.023}$	$8.58^{+0.04}_{-0.04}$
$\sigma_{10\,\rm keV}$	keV	$2.83^{+0.021}_{-0.021}$	$3.10^{+0.030}_{-0.029}$
$E_{\rm FeK\alpha}$	keV	$6.47^{+0.04}_{-0.04}$	$6.42^{+0.05}_{-0.06}$
$\sigma_{\rm FeK\alpha}$	keV	$0.36^{+0.07}_{-0.07}$	$0.54^{+0.09}_{-0.08}$
$\chi^2_{\rm red/dof}$		1.48 / 338	1.53 / 338

Notes. $^{(a)}$ Unabsorbed flux in the energy band from 3 to 50 keV, unit [keV s^{-1} cm^{-2}].
$^{(\dagger)}$ Fixed parameter.

Table 8: Best fit parameters of measurement $M2$ considering the different slopes of the peaks, with uncertainties given at 90% confidence level.

Parameter	increasing	decreasing	peak	off-peak	time-averaged
$N_{\rm H}$ [10^{22} cm^{-2}]	$1.5^{\dagger}$	$1.5^{\dagger}$	$1.5^{\dagger}$	$1.5^{\dagger}$	$1.5^{\dagger}$
$c_{\rm FPMA}$	$1^{\dagger}$	$1^{\dagger}$	$1^{\dagger}$	$1^{\dagger}$	$1^{\dagger}$
$c_{\rm FPMB}$	$0.9944^{\dagger}$	$0.9944^{\dagger}$	$0.9944^{\dagger}$	$0.9944^{\dagger}$	$0.9944^{\dagger}$
$E_{\rm CRSF,0}$ [keV]	$11.59^{\dagger}$	$11.59^{\dagger}$	$11.59^{\dagger}$	$11.59^{\dagger}$	$11.59^{\dagger}$
$\sigma_{\rm CRSF,0}$ [keV]	$1.91^{\dagger}$	$1.91^{\dagger}$	$1.91^{\dagger}$	$1.91^{\dagger}$	$1.91^{\dagger}$
$\tau_{\rm CRSF,0}$ [keV]	$0.79^{\dagger}$	$0.79^{\dagger}$	$0.79^{\dagger}$	$0.79^{\dagger}$	$0.79^{\dagger}$
$E_{\rm CRSF,1}$ [keV]	$23.35^{\dagger}$	$23.35^{\dagger}$	$23.35^{\dagger}$	$23.35^{\dagger}$	$23.35^{\dagger}$
$\sigma_{\rm CRSF,1}$ [keV]	$2.2^{\dagger}$	$2.2^{\dagger}$	$2.2^{\dagger}$	$2.2^{\dagger}$	$2.2^{\dagger}$
$\tau_{\rm CRSF,1}$ [keV]	$0.74^{\dagger}$	$0.74^{\dagger}$	$0.74^{\dagger}$	$0.74^{\dagger}$	$0.74^{\dagger}$
$E_{\rm CRSF,2}$ [keV]	$34.9^{\dagger}$	$34.9^{\dagger}$	$34.9^{\dagger}$	$34.9^{\dagger}$	$34.9^{\dagger}$
$\sigma_{\rm CRSF,2}$ [keV]	$1.7^{\dagger}$	$1.7^{\dagger}$	$1.7^{\dagger}$	$1.7^{\dagger}$	$1.7^{\dagger}$
$\tau_{\rm CRSF,2}$ [keV]	$0.71^{\dagger}$	$0.71^{\dagger}$	$0.71^{\dagger}$	$0.71^{\dagger}$	$0.71^{\dagger}$
$F_{\rm PL}{}^{a}$	$10.04^{+0.07}_{-0.08}$	$9.88^{+0.08}_{-0.08}$	$10.05^{+0.06}_{-0.06}$	$7.42^{+0.05}_{-0.05}$	$8.57^{+0.04}_{-0.04}$
$E_{\rm fold}$ [keV]	$9.14^{+0.15}_{-0.14}$	$9.39^{+0.17}_{-0.17}$	$9.25^{+0.12}_{-0.12}$	$9.54^{+0.13}_{-0.13}$	$9.40^{+0.09}_{-0.09}$
Γ	$0.437^{+0.018}_{-0.019}$	$0.480^{+0.020}_{-0.021}$	$0.453^{+0.015}_{-0.015}$	$0.497^{+0.015}_{-0.016}$	$0.476^{+0.011}_{-0.011}$
$F_{10\,\rm keV}{}^{a}$	$2.33^{+0.07}_{-0.07}$	$2.51^{+0.08}_{-0.08}$	$2.41^{+0.06}_{-0.06}$	$2.13^{+0.04}_{-0.04}$	$2.25^{+0.04}_{-0.04}$
$E_{10\,\rm keV}$ [keV]	$8.44^{+0.07}_{-0.07}$	$8.55^{+0.07}_{-0.08}$	$8.47^{+0.06}_{-0.06}$	$8.68^{+0.05}_{-0.05}$	$8.58^{+0.04}_{-0.04}$
$\sigma_{10\,\rm keV}$ [keV]	$3.10^{+0.06}_{-0.06}$	$3.13^{+0.06}_{-0.06}$	$3.12^{+0.05}_{-0.05}$	$3.08^{+0.04}_{-0.04}$	$3.10^{+0.030}_{-0.029}$
$E_{{\rm FeK}\alpha}$ [keV]	$6.42^{\dagger}$	$6.42^{\dagger}$	$6.42^{\dagger}$	$6.42^{\dagger}$	$6.42^{\dagger}$
$\sigma_{{\rm FeK}\alpha}$ [keV]	$0.54^{\dagger}$	$0.54^{\dagger}$	$0.54^{\dagger}$	$0.54^{\dagger}$	$0.54^{\dagger}$
$\chi^2_{\rm red/dof}$	1.31 / 351	1.16 / 350	1.24 / 361	1.26 / 360	1.53 / 338

Notes. $^{(a)}$ Unabsorbed flux in the energy band from 3 to 50 keV, unit [keV s^{-1} cm^{-2}].
$^{(\dagger)}$ Fixed parameter.

References

Becker P.A., Klochkov D., Schönherr G., et al., 2012, A&A 544, A123

Becker P.A., Wolff M.T., 2007, ApJ 654, 435

Bildsten L., Chakrabarty D., Chiu J., et al., 1997, ApJS 113, 367

Charley S., 2013, Test magnet reaches 13.5 tesla – a new CERN record, https://home.cern/news/news/engineering/test-magnet-reaches-135-tesla-new-cern-record Zugriff am 2019-02-11

Clayton D.D., 1968, Principles of stellar evolution and nucleosynthesis, McGraw-Hill, New York

Coburn W., 2001, Ph.D. thesis, UNIVERSITY OF CALIFORNIA, SAN DIEGO

Crampton D., 1974, ApJ 187, 345

Deeter J.E., Boynton P.E., Pravdo S.H., 1981, ApJ 247, 1003

Ferrigno C., Becker P.A., Segreto A., et al., 2009, A&A 498, 825

Ferrigno C., Falanga M., Bozzo E., et al., 2011, A&A 532, A76

Gehrels N., 1986, ApJ 303, 336

Giacconi R., Gursky H., Kellogg E., et al., 1971, Astrophys. J., Lett. 167, L67

Giacconi R., Gursky H., Paolini F.R., Rossi B.B., 1962, Phys. Rev. Lett. 9, 439

Giacconi R., Murray S., Gursky H., et al., 1972, ApJ 178, 281

Girardi L., Bressan A., Bertelli G., Chiosi C., 2000 141, 371

Grinberg V., Hell N., El Mellah I., et al., 2017, A&A 608, A143

Harrison F.A., Craig W.W., Christensen F.E., et al., 2013, ApJ 770

Heindl W.A., Coburn W., Gruber D.E., et al., 2000, In: McConnell M.L., Ryan J.M. (eds.) American Institute of Physics Conference Series, Vol. 510. American Institute of Physics Conference Series, p.173

Heindl W.A., Coburn W., Gruber D.E., et al., 1999, Astrophys. J., Lett. 521, L49

Iben, Icko J., 1991, ApJS 76, 55

Iyer N., Mukherjee D., Dewangan G.C., et al., 2015, MNRAS 454, 741

Jin Y.K., Zhang S.N., Wu J.F., 2006, ApJ 653, 1566

Klochkov D., Staubert R., Postnov K., et al., 2008, A&A 482, 907

Koyama K., Tsunemi H., Dotani T., et al., 2007, PASJ 59, 23

Lamb F.K., Pethick C.J., Pines D., 1973, ApJ 184, 271

Lampton M., Margon B., Bowyer S., 1976, ApJ 208, 177

Lattimer J.M., Prakash M., 2004, Science 304, 536

Lotti S., Natalucci L., Mori K., et al., 2016, ApJ 822, 57

Madsen K.K., Harrison F.A., Markwardt C.B., et al., 2015, ApJS 220, 8

Motta S.E., Rouco Escorial A., Kuulkers E., et al., 2017, MNRAS 468, 2311

Müller S., Ferrigno C., Kühnel M., et al., 2013, A&A 551, A6

Nagel W., 1980, ApJ 236, 904

Nakajima M., Mihara T., Makishima K., Niko H., 2006, ApJ 646, 1125

Nakamura D., Ikeda A., Sawabe H., et al., 2018, Review of Scientific Instruments 89, 095106

Negueruela I., Okazaki A.T., 2001, A&A 369, 108

Park T., Kashyap V.L., Siemiginowska A., et al., 2006, ApJ 652, 610

Press W.H., Teukolsky S.A., Vetterling W.T., Flannery B.P., 1992, NUMERICAL RECIPES IN C: THE ART OF SCIENTIFIC COMPUTING, Press Syndicate of the University of Cambridge

Roy J., Agrawal P.C., Iyer N.K., et al., 2019, ApJ 872, 33

Sasaki M., Müller D., Kraus U., et al., 2012, A&A 540, A35

Schwarm F.W.M., 2017, Ph.D. thesis, Friedrich-Alexander-Universität Erlangen-Nürnberg

Shaw A., Charles P., 2013, Astronomy and Geophysics 54, 6.22

Soong Y., Swank J.H., 1989, In: Hunt J., Battrick B. (eds.) Two Topics in X-Ray Astronomy, Volume 1: X Ray Binaries. Volume 2: AGN and the X Ray Background, Vol. 296. ESA Special Publication

Tananbaum H., Gursky H., Kellogg E.M., et al., 1972, Astrophys. J., Lett. 174, L143

Trümper J., Pietsch W., Reppin C., et al., 1978, Astrophys. J., Lett. 219, L105

Tsygankov S., Lutovinov A., 2007, In: JENAM-2007, "Our Non-Stable Universe"., p.40

Verner D.A., Yakovlev D.G., 1995, A&AS 109, 125

Wilms J., Allen A., McCray R., 2000, ApJ 542, 914

Erklärung

Hiermit erkläre ich, dass ich die vorliegende Bachelorarbeit selbstständig verfasst und keine außer den angegebenen Quellen und Hilfsmitteln verwendet habe.

Datum, Ort

Unterschrift